Calibration of the shear-modified GTN model for HAZ of butt-welded high-strength steel (HSS)

Gao, Yize; Yan, Rui; Veljkovic, Milan; Mela, Kristo; Li, Guo Qiang; Wang, Yan Bo; Zhao, Xiao Ling

DOI
10.1016/j.tws.2025.114027

Publication date
2025

Document Version
Final published version

Published in
Thin-Walled Structures

Citation (APA)
Gao, Y., Yan, R., Veljkovic, M., Mela, K., Li, G. Q., Wang, Y. B., & Zhao, X. L. (2025). Calibration of the shear-modified GTN model for HAZ of butt-welded high-strength steel (HSS). *Thin-Walled Structures*, *218*(Pt. B), Article 114027. https://doi.org/10.1016/j.tws.2025.114027

Thin–Walled Structures 218 (2026) 114027

Contents lists available at ScienceDirect

Thin-Walled Structures

journal homepage: www.elsevier.com/locate/tws

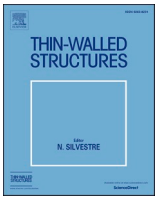

Calibration of the shear-modified GTN model for HAZ of butt-welded high-strength steel (HSS)

Yize Gao [a,b], Rui Yan [b], Milan Veljkovic [c], Kristo Mela [d], Guo-Qiang Li [a], Yan-Bo Wang [a], Xiao-Ling Zhao [b,*]

[a] College of Civil Engineering, Tongji University, Shanghai, China
[b] Department of Civil and Environmental Engineering, The Hong Kong Polytechnic University, Hong Kong, China
[c] Department of Engineering Structures, Delft University of Technology, Delft,
[d] Faculty of Built Environment, Tampere University, Tampere, Finland

ARTICLE INFO

Keywords:
GTN model
Shear tests
Heat-affected zone
High-strength steel

ABSTRACT

Welding induces microstructural changes in the base metal, forming a heat-affected zone (HAZ) that is especially prone to strength degradation in high-strength steel (HSS) connections. While the mechanical behavior of welded joints is strongly influenced by the softened HAZ, most existing research has focused on its tensile and fatigue properties, with limited attention given to its shear behavior, despite evidence of shear failure mechanisms in certain welded structures.

Building on recent advances in damage modeling, this paper calibrates a shear-modified Gurson-Tvergaard-Needleman (GTN) model tailored for the HAZ. The GTN model, which uses void volume fraction as a damage index and accounts for microvoids and stress triaxiality, is extended here to better capture shear-dominated failure modes. In the meantime, shear tests were conducted on coupon specimens extracted from butt-welded cold-formed rectangular hollow sections fabricated from three steel grades and three thicknesses. Load-deformation curves and local strain measurements are obtained from these shear tests. Finite element (FE) simulations of the HAZ, incorporating the shear-modified GTN model, are conducted. The experimentally measured load-deformation curves are used to calibrate the parameters of the shear-modified GTN model, while the measured local strains serve to validate the FE model. Practical values for the key parameters of the shear-modified GTN model are recommended for engineering applications. The estimated ultimate load carrying capacity based on the proposed model is in close agreement (approximately 5 %) with the experimental values. The limitations of the proposed model and directions for future research are also pointed out.

1. Introduction

Welding is widely employed to join steel members. The heating and cooling process during welding induces microstructural changes in the base metal (BM) adjacent to the welds, resulting in the formation of a heat-affected zone (HAZ) [1–4]. Strength degradation within the HAZ becomes increasingly pronounced with higher steel grades, particularly in high-strength steel (HSS) connections [3,5–10].

The strength of the softened HAZ is a critical factor in determining the mechanical behavior of welded joints. Hardness measurements reveal the inhomogeneity of the HAZ [1,3,5], which partially reflects changes in strength but does not fully capture the mechanical response. Some studies have calibrated equivalent HAZ models using coupon tests and finite element (FE) analyses of welded connections [11,12]. However, most investigations of the HAZ in butt-welded joints have focused on tensile strength [4,7,13–15] and fatigue strength [16–19]. Research on the shear behavior of the HAZ is limited, despite the identification of shear failure mechanisms in HAZ, such as those observed in tubular joints [20–22]. To address this gap, the present study investigates the shear behavior of the HAZ in butt-welded HSS connections through shear tests on the HAZ and calibrates a damage model to account for shear effects.

Recent studies on shear-induced damage in HSS, particularly those based on punch-shear or blanking tests, have shown that the fracture surface typically comprises the rollover zone, shear zone, fracture zone, and burr zone, where micro-defects tend to develop into microcracks

* Corresponding author.
E-mail address: xiao-lin.zhao@polyu.edu.hk (X.-L. Zhao).

https://doi.org/10.1016/j.tws.2025.114027
Received 4 May 2025; Received in revised form 23 September 2025; Accepted 24 September 2025
Available online 24 September 2025

Table 1
Summary of the parameters and calibration method.

Parameters	Definition	Calibration
q_1, q_2	Parameters to measure the influence of VVF on the GTN field surface	Calibrated by tensile tests from the same welded joints [20].
f_0	Initial VVF	
f_c	Critical VVF at the onset of rapid increase	
f_f	VVF when the element is deleted with only microvoid evolution	
c, d, K	Parameters to modify the Lode dependence function	Calibrated by tensile, shear, compression and tortion tests in the previous study [54].
T	Parameters to modify the failure criterion of Eq. (8)	
D_0	Initial shear damage	Parameters calibrated in this study
D_f	Shear damage when the element is deleted with only shear damage evolution	
k_ω	Parameters to measure the rate of shear damage increase	

Table 2
Parameters calibrated based on previous studies.

Parameters	S355	S500	S700
$q_1=Af^B$	A= 1.443; B=−0.068	A= 1.417; B=−0.079	A= 1.443; B=−0.068
q_2		1.015	
f_0		0.001	
f_c	0.03288	0.02257	0.01650
f_f		0.05	
f_u		$=1/q_1$	
c, d, K		c = 0.83, d = 0.5, K=−0.3	

[23,24]. Among mechanical models incorporating microscale damage mechanisms, the Gurson-Tvergaard-Needleman (GTN) model [25–29] uses the void volume fraction (VVF) as a damage index and performs well under tension-dominated stress states [28,30–36]. However, the GTN model demonstrates certain limitations in capturing the mechanical behavior under shear-dominated stress conditions [37–39], leading to many studies focusing on incorporating shear damage modifications into the GTN model [40–50]. Existing shear-modified GTN models have certain limitations in application as discussed in Section 2.1 and do not address the HAZ. This study aims to fill this knowledge gap by refining and calibrating a shear-modified model for the HAZ.

This paper calibrates a shear-modified GTN model for the HAZ, with key parameters identified and subsequently determined. Butt-welded cold-formed rectangular hollow sections with three different steel grades and three thicknesses are fabricated to produce coupon specimens for shear testing of the HAZ. Load-deformation curves and local strain measurements are obtained from these shear tests. Finite element (FE) simulations of the HAZ, incorporating the shear-modified GTN model, are conducted. The experimentally measured load-deformation curves are used to calibrate the parameters of the shear-modified GTN model, while the measured local strains serve to validate the FE model. Practical values for the key parameters of the shear-modified GTN model are proposed. The estimated ultimate load-carrying capacity based on the proposed model closely matches the experimental results, with discrepancies of approximately 5 %. The limitations of the proposed model and directions for future research are also pointed out.

2. Shear-modified GTN model

2.1. The shear-modified GTN model for calibration

The HAZ with limited area and material heterogeneity is idealized as an equivalent homogeneous area for analysis. Previous studies have demonstrated that the GTN model calibrated by the tensile tests of HAZ specimens can reproduce the mechanical behaviour of the welded connections with good agreement between numerical simulations and experimental results [20,51]. To consistently characterize the HAZ mechanical behaviour across different stress states, a shear-modified GTN model is further studied and calibrated to capture HAZ damage under shear-dominated stress states.

Table 3
Information on seven loading cases in the unit cell.

Stress state		Uniaxial tensile	Pure shear	Tensile shear				
Reference figure		Fig. 1(a)		Fig. 1(b)				
U1/U2		–	0	0.25	0.5	1	2	4
Node coordinates	(0,0,0)	Ux=0, Uy=0		Ux=0, Uy=0				
	(1,0,0)	Ux=U1, Uy=0		Ux=U1, Uy=U2				
	(1,1,0)	Ux=U1		Ux=U1, Uy=U2, Uz=0				
	(0,1,0)	Ux=0		Ux=0, Uy=0				
	(0,0,1)	Ux=0, Uy=0 Uz=0		Ux=0, Uy=0 Uz=0				
	(1,0,1)	Ux=U1, Uy=0 Uz=0		Ux=U1, Uy=U2 Uz=0				
	(1,1,1)	Ux=U1		Ux=U1, Uy=U2 Uz=0				
	(0,1,1)	Ux=0		Ux=0, Uy=0, Uz=0				

Table 4
Parameters used in the trial unit.

f_0	f_c	f_f	D_0	D_f	k_ω	T
0.001	0.0165	0.05	0.004	0.04	1	0.1

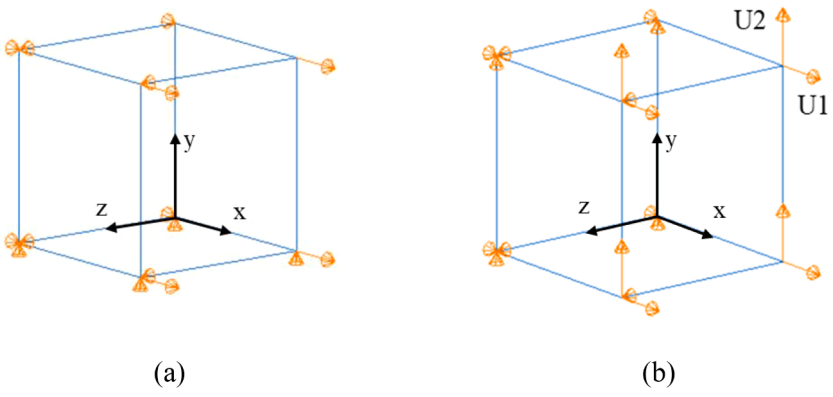

(a) (b)

Fig. 1. Boundary conditions of (a) unit tensile, (b) pure shear and tensile-shear states.

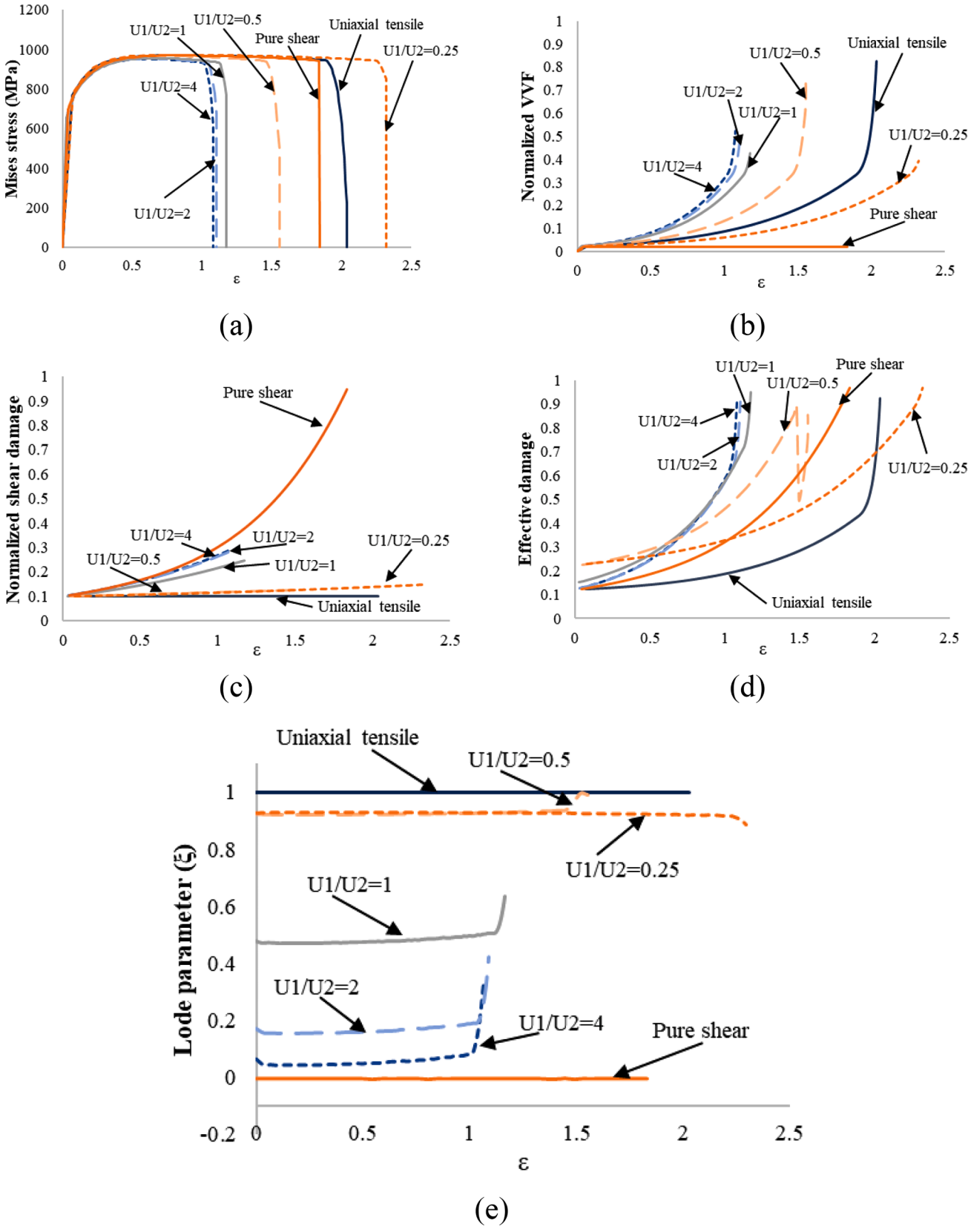

Fig. 2. (a) Mises stress versus equivalent strain and evolution of (b) normalized VVF, (c) shear damage and (d) effective damage of different loading conditions (e) development of ξ.

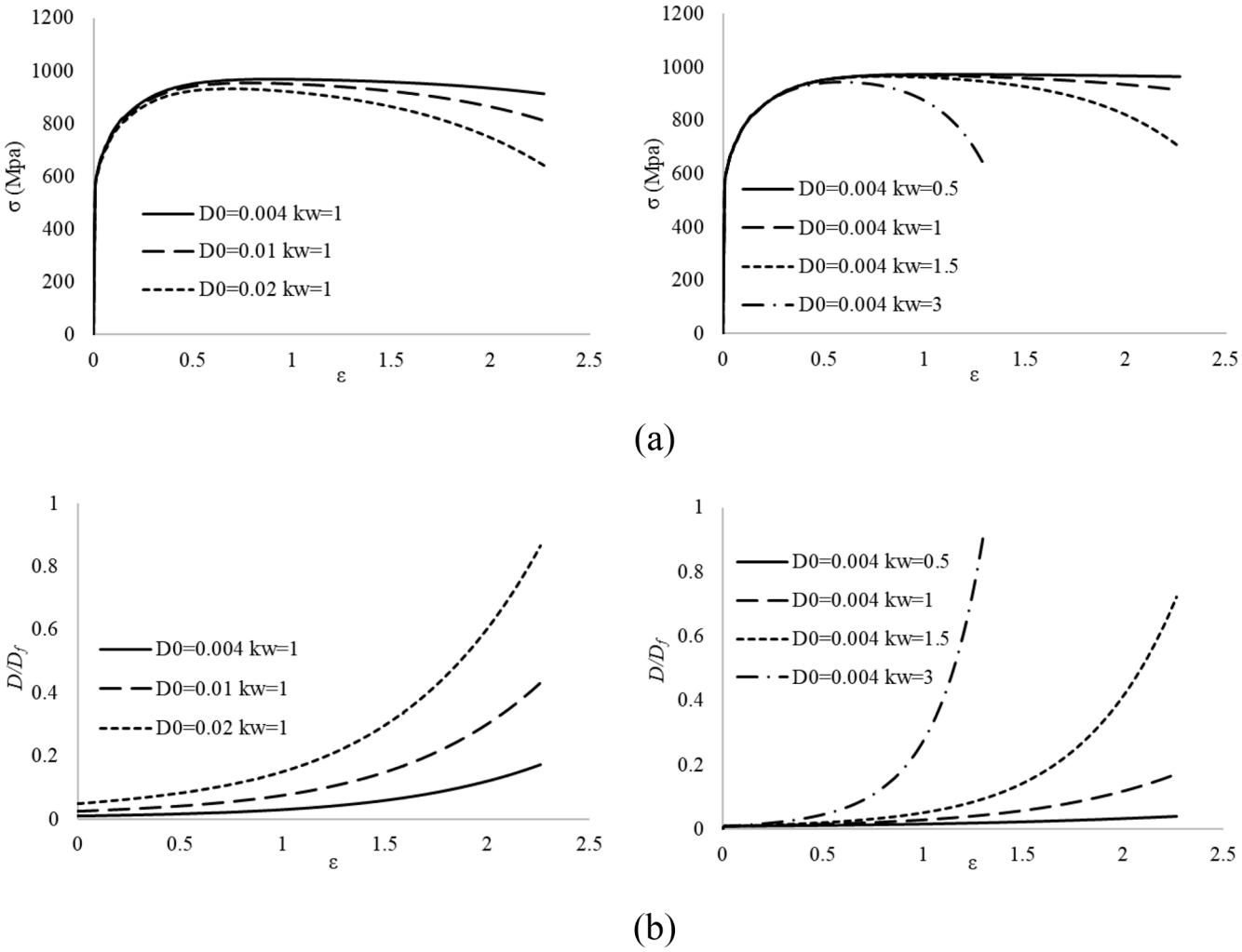

Fig. 3. (a) Mises stress - equivalent strain and (b) shear damage evolution of pure shear unit with different parameters.

Table 5
Nominal dimensions of hollow sections.

Code name	Steel grade	Profile	Wall thickness t [mm]	Outer corner radius r [mm]
S355t5	S355	100×50×5	5	9
S355t8		140×140×8	8	20
S355t10		160×160×10	10	25
S500t4	S500	140×140×4	4	8.5
S500t8		140×140×8	8	20
S500t10		160×160×10	10	25
S700t5	S700	120×120×5	5	9
S700t8		120×120×8	8	20
S700t10		120×120×10	10	25

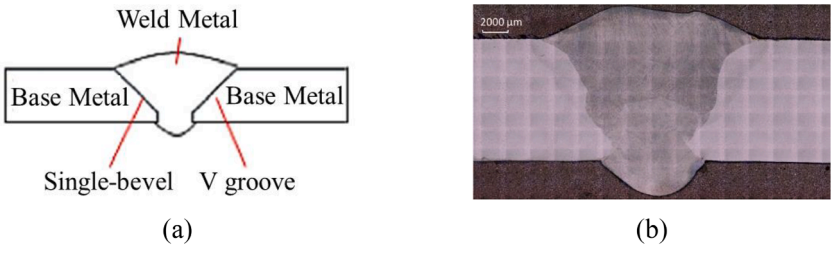

Fig. 4. (a) The schematic drawing of the cross-section. (b) The etched cross-section of S500MH welded connection (10 mm).

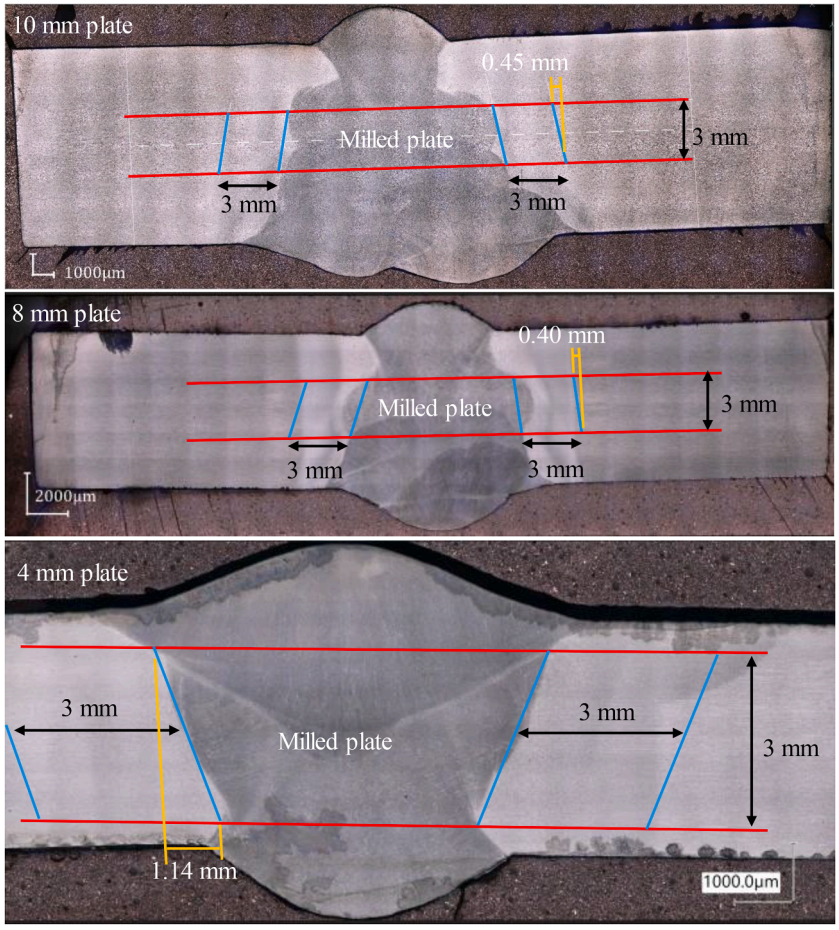

Fig. 5. Inclined HAZ in the weld cross-sections.

Table 6
The determined width of HAZ and WM [mm].

Steel grade	S355			S500			S700		
Thickness	t5	t8	t10	t4	t8	t10	t5	t8	t10
HAZ1	4.0	3.0	3.0	5.0	4.0	4.0	3.0	3.0	3.5
HAZ2	3.5	3.5	4.0	4.0	4.0	3.5	3.0	3.0	2.5
WM	12.0	14.0	11.5	4.0	9.0	9.0	7.5	9.5	9.0

2.1.1. *Shear damage evolution uncoupled with VVF*

Shear-modified GTN models that incorporates the shear damage evolution into VVF development generally have large variations in calibration across different states and tend to over-predict damage at high porosity [45,48–50]. Therefore, the shear damage model uncoupled with VVF is adopted in this study to enhance reliability [52–57]. Although the GTN model use damage indexes based on microscale mechanism, it is rather difficult to quantify the voids and cracks at the micro level. Hence, the material behaviour at the macro level is employed to quantify the effect of shear damage on mechanical response. This paper draws on the models of Jiang et al [53] and Wu et al [54], adopting a shear damage evolution theory based on the macro-mechanical test results, as illustrated in Eq. (4), where $\omega'(\theta)$ is the modified Lode dependence function describing the effects from Lode angle (θ) or Lode parameters (ξ), $\boldsymbol{S}$ is the deviatoric stress tensor and k_ω is the parameter need to be determined to control the shear damage evolution rate. Due to the lack of sufficient experimental evidence, assumptions regarding shear damage coalescence and nucleation are not considered.

2.1.2. *Lode dependence function*

Eq. (5) modified by previous studies [53,54] was employed as the Load dependence function in order to include the various stress states, where c, d and K are the parameters calibrated by mechanical tests in general compression stress states and $\xi = 27J_3/2q^3$. When stress triaxiality (η) is negative, the value of the function gradually decreases with the reduction of η until reaching the defined lower limit. For positive η, the function remains consistent with the formulation proposed by

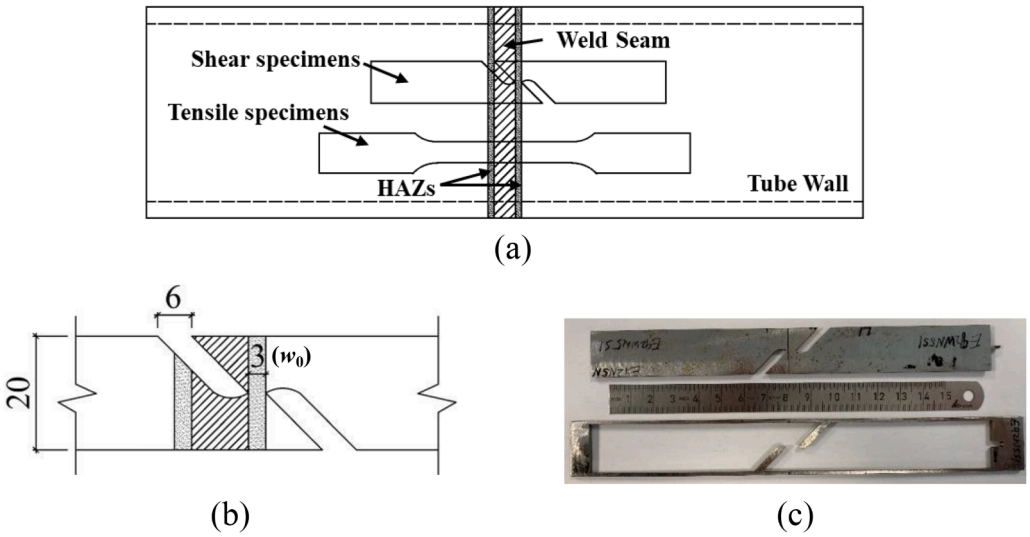

Fig. 6. (a) Specimen cutting scheme from different profiles. (b) Shear specimen dimensions (unit in mm). (c) The shear specimen cut from S700t8.

Table 7
Initial dimensions of the shear segment in specimens.

Specimen code	S355t5_1	S355t5_2	S355t8	S355t10_1	S355t10_2
Thickness[mm]	3.01	3.04	3.02	3.02	3.03
w_0[mm]	3.25	3.25	3.25	3.25	3.53
A_0[mm^2]	9.79	9.88	9.83	9.82	10.69
Specimens code	S500t4	S500t8_1	S500t8_2	S500t10_1	S500_t10_2
Thickness[mm]	2.96	3.03	3.03	3.02	3.03
w_0[mm]	3.26	3.25	3.02	3.01	3.75
A_0[mm^2]	9.65	9.85	9.15	9.08	11.38
Specimens code	S700t5	S700t8_1	S700t8_2	S700t10	
Thickness[mm]	2.96	2.93	2.98	3.04	
w_0[mm]	3.25	3.02	3.50	3.00	
A_0[mm^2]	9.61	8.99	10.64	9.00	

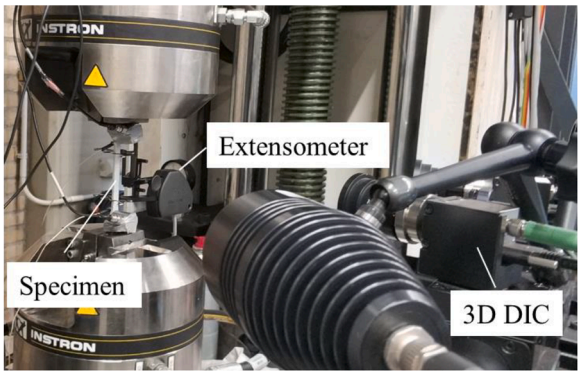

Fig. 7. Experimental setup.

Nahshon and Hutchinson [41].

2.1.3. Fracture criteria

In the FE model utilizing the original GTN, an element is deleted when its VVF reaches the value of f_f. Wu et al [54] and He et al [58] both defined the effective damage (D_{eff}) based on the sum of the normalized VVF and normalized shear damage, which is suitable for complex damage evolution that includes both shear damage and VVF evolution. The piecewise function adopted in Wu's model [54] considers the influence of η and Lode parameters. However, this piecewise function may cause the mutations of the D_{eff} value. Therefore, Eq. (7) and Eq. (8), referring to [58] and [54], are discussed in the following Sections 2.2 and 5.2 to determine the fracture criterion. In addition to maintaining consistency with the original GTN model calibrated by a series of tensile tests, critical VVF (f_c) is replaced by fracture VVF (f_f) in the following study.

2.1.4. Yield function

The yield function proposed by Wu et al [54] avoids the coupling between shear damage and hydrostatic stress (p), and has been validated for various complex stress states. Therefore, the yield function in Eq. (1) was adopted.

To conclude, the shear-modified GTN model employed in this study is adopted from Jiang et al [53] and Wu et al [54] with minor modifications (excluding shear damage nucleation and coalescence). The detailed equations are presented in Eq. (1)-(6). The shear-modified GTN model incorporates two decoupled damage evolution mechanisms. The damage from VVF evolution (f^*) is driven by volumetric strain increment as Eq. (2) shows, and dominates the damage evolution primarily under stress states with high stress triaxiality. The shear damage (D) is governed by the deviatoric stress components and modulated by the Lode parameter, as Eq. (4) illustrates. Under tension-dominated loading conditions (e.g., uniaxial or triaxial tension), damage evolution is primarily governed by VVF. In contrast, under pure shear conditions where volumetric strain is negligible, only shear damage would develop. The parameters related to the shear modified-GTN model and determining process are summarized in Table 1, and the corresponding values are illustrated in Table 2.

$$\Phi = \frac{q^2}{(1-D)^2\sigma_{my}^2} + 2q_1 f^* \cosh\left(-\frac{3q_2 p}{2\sigma_{my}}\right) - 1 - (q_1 f^*)^2 \tag{1}$$

Where:

$$p = -\frac{1}{3}\boldsymbol{\sigma} : \boldsymbol{I},\ q = \left(\frac{3}{2}\boldsymbol{S} : \boldsymbol{S}\right)^{\frac{1}{2}},\ \boldsymbol{S} = \boldsymbol{\sigma} + p\boldsymbol{I}$$

$\boldsymbol{\sigma}$ and $\boldsymbol{S}$ are the material's stress tensor and deviatoric stress tensor, respectively. $\boldsymbol{I}$ is the identity matrix. q, p and σ_{my} are the von Mises equivalent stress, hydrostatic stress, and the flow stress of the undamaged matrix material from the isotropic hardening model, respectively.

$$\dot{f} = (1-f)\dot{\boldsymbol{\varepsilon}}^p : \boldsymbol{I} \tag{2}$$

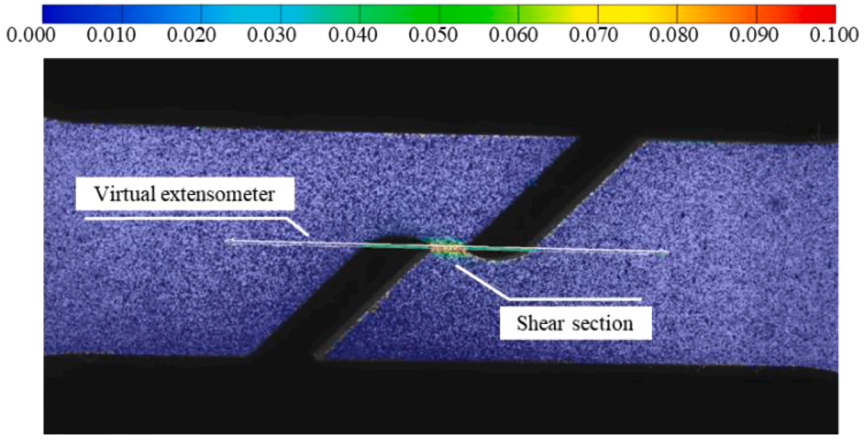

(a)

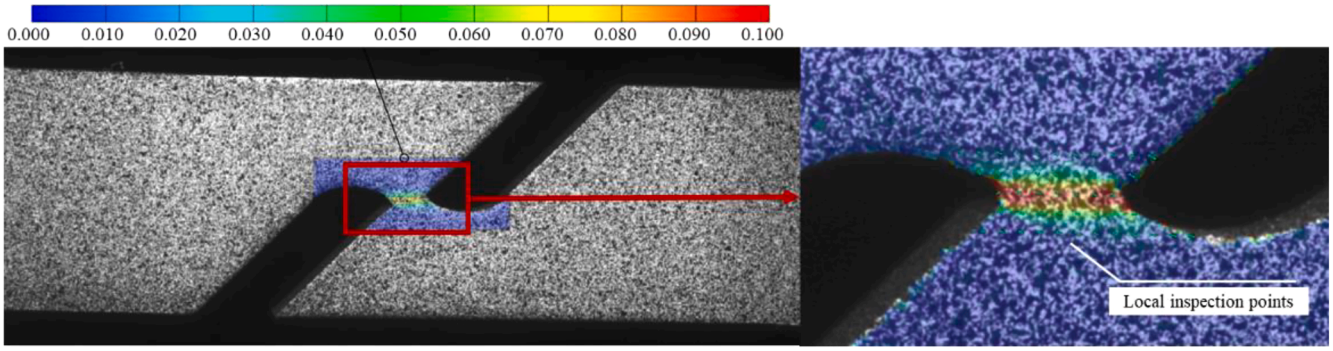

(b)

Fig. 8. Equivalent strain map of S700t5 (a) global surface and (b) around the shear segment.

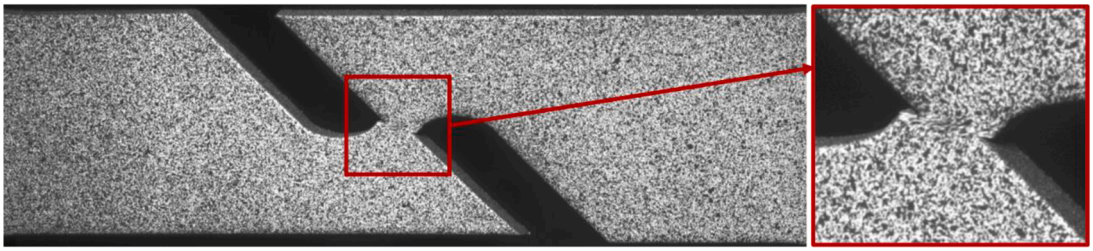

Fig. 9. Failure of shear test specimens (S700t10).

$$f^*(f)=\begin{cases}0 & f\le 0\\ f & f\in[0,f_c]\\ f_c+\dfrac{f_u-f_c}{f_f-f_c}(f-f_c) & f\in\left(f_c,f_f\right)\\ f_u & f\in\left[f_f,+\infty\right)\end{cases} \tag{3}$$

$$\dot{D}=k_\omega D\omega'(\theta)\frac{\boldsymbol{S}:\dot{\boldsymbol{\varepsilon}}^{\boldsymbol{p}}}{q} \tag{4}$$

$$\omega'(\theta)=\begin{cases}\left(1-\xi^2\right)(1+cK)^2-dK & (\eta<K)\\ \left(1-\xi^2\right)(1+c\eta)^2-d\eta & (K\le\eta\le 0)\\ 1-\xi^2 & (\eta>0)\end{cases} \tag{5}$$

$$\dot{\bar{\varepsilon}}_m^p=\frac{\boldsymbol{\sigma}:\dot{\boldsymbol{\varepsilon}}^{\boldsymbol{p}}}{(1-f)(1-D)\sigma_{my}} \tag{6}$$

$$D_{eff}=\frac{f}{f_f}+\frac{D}{D_f} \tag{7}$$

$$D_{eff}=\begin{cases}\dfrac{f}{f_f}+\dfrac{D}{D_f}=1 & (\eta\le 0)\\ \dfrac{f}{f_f}+\dfrac{D}{D_f}=1 & (\omega'\le T,\eta>0)\\ [2-\omega'(\theta,\eta)]\left(\dfrac{f}{f_f}+\dfrac{D}{D_f}\right)=1 & (\omega'>T,\eta>0)\end{cases} \tag{8}$$

2.2. Determination of fracture criterion and parametric study of the modified-GTN model

A unit cell with one C3D8R element assigned is employed to investigate the effect of each parameter on the mechanical behaviour and

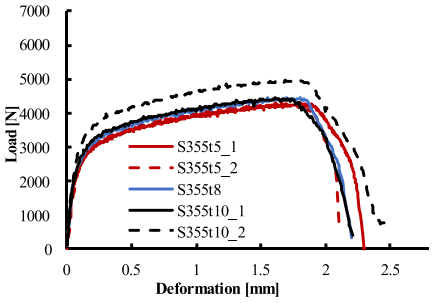

(a) S355.

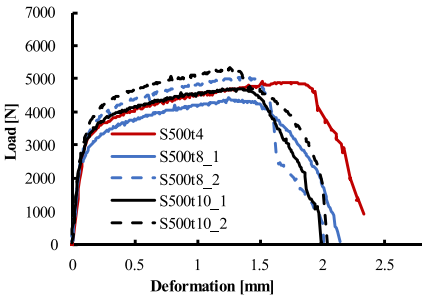

(b) S500.

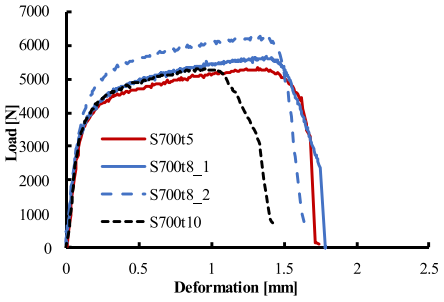

(c) S700.

Fig. 10. Load - deformation curves of shear tests.

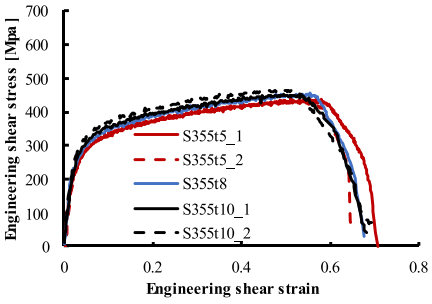

(a) S355.

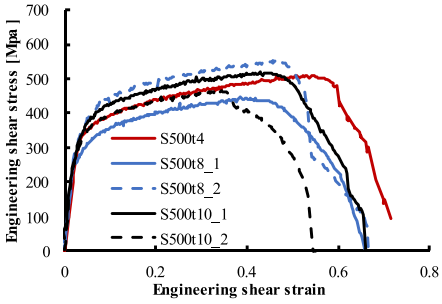

(b) S500.

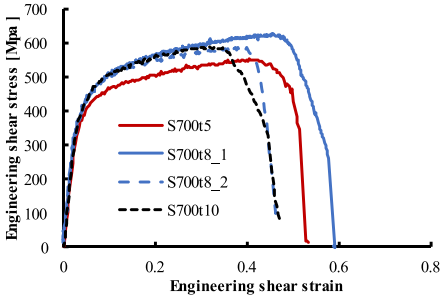

(c) S700.

Fig. 11. τ -ε_{es} curves of shear tests.

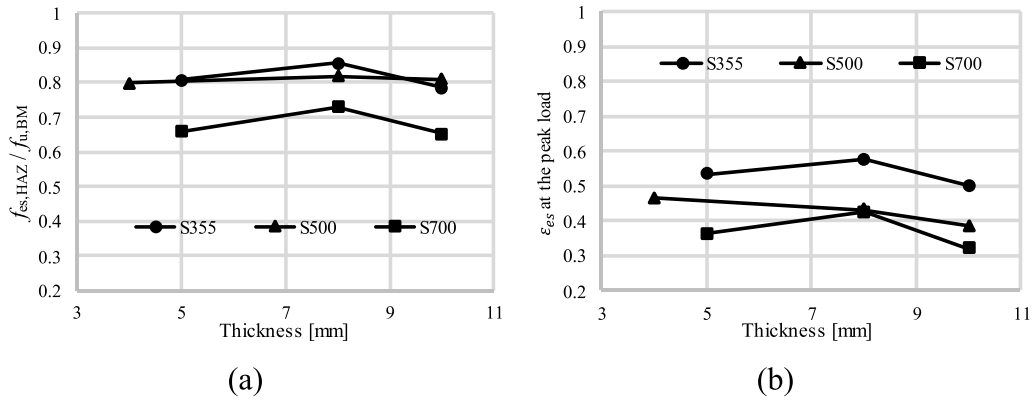

Fig. 12. (a) ratio of engineering shear strength of HAZ to ultimate strength of BM and (b) engineering shear strain corresponding to the peak load.

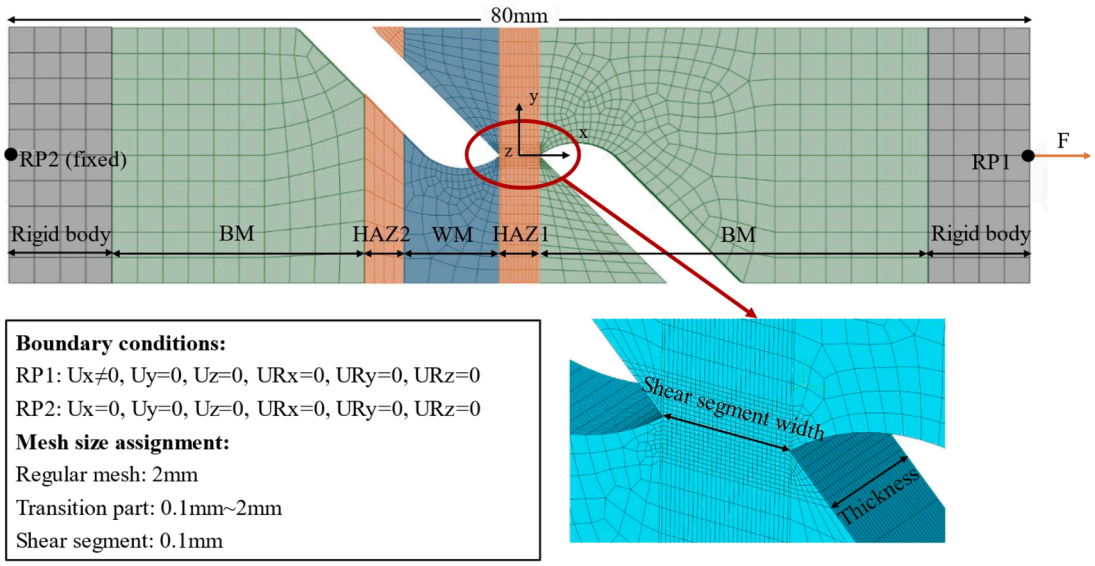

Fig. 13. Model of specimens assigned with different properties.

damage evolution of the shear-modified GTN model under different stress states with the fracture criterion of Eq. (8).

Seven different boundary conditions were used to identify the material behaviour of the modified model. The boundary conditions of uniaxial tension, shear and tensile-shear (a combination of tension and shear) are set as illustrated in Fig. 1(a) and (b) respectively. U1 and U2 represent the displacements in the x and y directions, respectively, and the ratios of U1/U2 are shown in Table 3. As the U1/U2 increases, volumetric strain (driving the evolution of VVF) becomes more dominant. In contrast, when U1/U2 decreases, shear strain (affecting the development of shear damage) is more significant. Table 3

The calibrated parameters reported in [33,54] are adopted in this calculation, as listed in Table 4.

The Mises stress, normalized VVF, shear damage, and Lode parameters (ξ) versus equivalent strain (ε) of all conditions are depicted in Fig. 2.

Fig. 2(a) shows that most of the units in tension-shear states are fully damaged earlier with a sharply decreased strength, compared to that in the uniaxial tensile state. As for U1/U2=0.25, slower increases in VVF and shear damage are observed in Fig. 2(b) and (c), resulting in the slower D_{eff} increase and late element deletion even with the multiplier (2-ω') which is higher than 1.

It can be seen from Eq. (2) that only the growth of plastic volume affects the development of VVF. However, both normalized deviatoric stress plastic work and ξ affect the evolution of shear damage. For instance, the curves of U1/U2 = 2, 1, 0.5 in Fig. 2(c) and (e) depict that, the normalized shear damage increases with the equivalent strain, and a larger ξ also indicates a smaller shear damage increasing rate. Therefore, in circumstances with minor plastic volume growth and ξ near unity, it would be difficult to reach the deletion point even with large deformation. The multiplier which is higher than unity is employed to accelerate the D_{eff} increase when ω' is higher than a certain value, which can be seen from the different initial D_{eff} in Fig. 2(d). However, except for uniaxial tensile and pure shear cases, the Lode parameters in other items will change during the displacement loading process (Fig. 2(e)), which reveals that the mutation of effective damage D_{eff} may occur unreasonably in the loading process, as the line 'U1/U2=0.5 Deff' shown in Fig. 2(d).

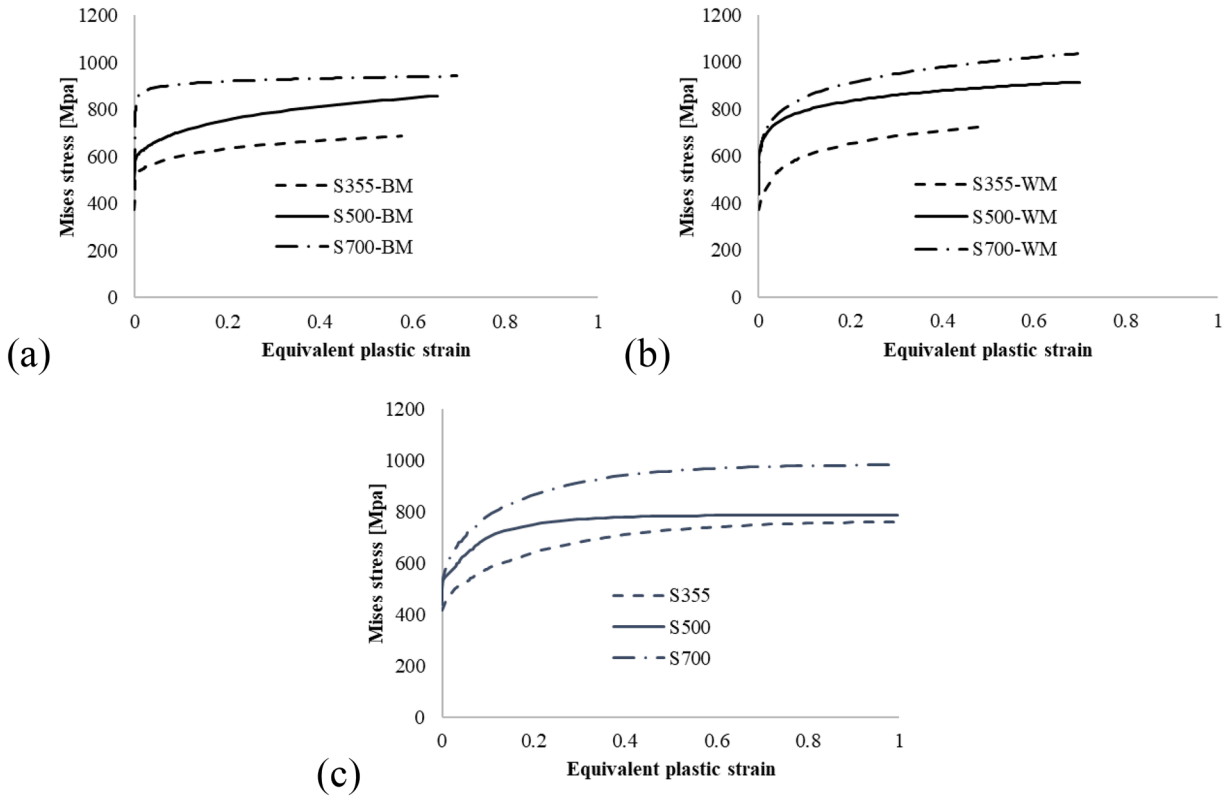

Fig. 14. True stress-plastic true strain relationships of (a) BM, (b) WM and (c) Undamaged true stress-plastic true strain relationships of HAZ.

A stepped part will occur in the descending stage of the load-displacement curve as shown in Fig. 20 in Section 5 after the fracture starts. There is a large shear damage gradient and VVF gradient near the edge of the shear segment, where the fracture initiates. Meanwhile, a large gradient of the Lode parameter also exists. If the non-differentiable piecewise D_{eff} is adopted and accelerate the deletion of elements in the stepped part, the discontinuity of the deletion will be amplified, that is, after the edge of the unit is deleted, it will take a longer loading period for the elements in the middle part to be deleted, leading to unreasonable stepped post-fracture curves.

Therefore, a modified definition of D_{eff} (Eq. (7)) is proposed, where the multiplier is abandoned. The mutation of D_{eff} and the stepped part when fracture happens can be avoided.

In the state of pure shear stress, which is only affected by shear damage parameters, the effects of D_0 and k_ω on the stress-strain relationship and damage development are shown by changing their values as depicted in Fig. 3. A larger D_0 will cause the strength reduction upon entering the plastic stage, while the effect of k_ω will be distinct after enough accumulation of shear damage. Finally, the value of D_f is used to control the deleted status of the unit.

3. Shear tests on HAZ

3.1. Materials and specimens

In this research, 9 types of butt-welded cold-formed RHS connections with 3 different steel grades (S355J2H, S500MH, and S700MLH, technical terms of delivery EN10219–1 [59]) and 4 different wall thicknesses (4 mm / 5 mm, 8 mm, 10 mm) were fabricated to produce the shear specimens. Five welded tubes were fabricated for each type. Table 5 contains the nominal dimensions of the profiles, the thickness (t), and the outer corner radius (r) of the hollow sections. Full penetration welding was performed on two single-V bevelled tubes (45° with a 1 mm gap at the root). A schematic drawing and etched cross-section are presented in Fig. 4. The metal active gas welding (MAGW) was conducted at an ambient temperature of 20 °C, with an interpass temperature lower than 200 °C. At least two welding passes (a root and a cap pass) were applied, except for the 10 mm thick tube where four welding passes (a root, a fill, and two cap passes) were applied. The heat input ranged from 1.0 kJ/mm to 1.4 kJ/mm, with the shield gas containing 60 % Ar, 30 % He, and 10 % CO_2. The filler metal Cartbofil 1 was used for S355, while Union NiMoCr was employed for S500 and S700.

Shear specimens were fabricated from the tube wall opposite to the longitudinal weld of the cold-formed tubes, as depicted in Fig. 6(a). Firstly, the tube wall was cut from the tube and milled to a central layer of 3 mm. Afterwards, hardness tests were conducted on the milled plate (Fig. 5(c)) prior to specimen cutting. The region of HAZ was marked on the milled plate, and specimens were cut in a way that the shear segment is on the marked HAZ region to ensure the failure in HAZ. The widths of weld metal (WM) and HAZs on both sides (HAZ1 and HAZ2) determined in previous study [11] were adopted in this paper, as presented in Table 6. Fig. 5 presents the region of milled plates (within red lines) and the 3 mm assumed HAZs (within blue lines) of three examples with 10 mm, 8 mm, and 4 mm thickness. It can be seen that HAZs' position on the top and bottom surfaces of the plate varies significantly. However, the variation of HAZs' position in the central 3 mm layer is limited, which are 0.45 mm, 0.40 mm, and 1.14 mm for plates with the thickness of 10 mm, 8 mm, and 4 mm, respectively. The shear segment is designed

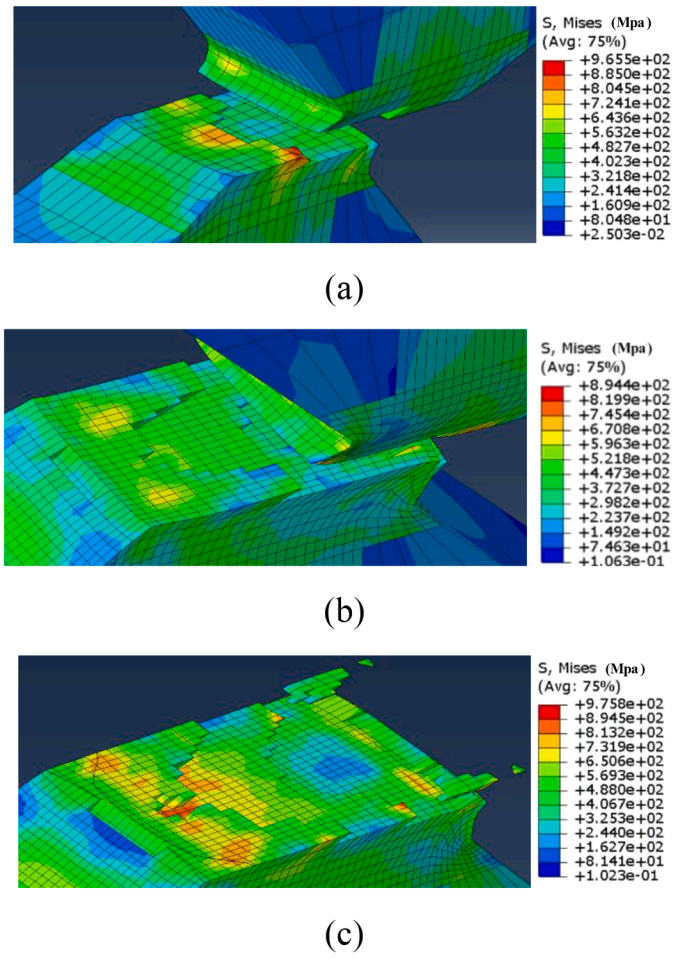

Fig. 15. Fracture surface with different mesh sizes of (a) 250 μm (b) 125 μm (c) 100 μm.

to be 3 mm as shown in Fig. 6(b), which is smaller than the determined width shown in Table 6, especially that 4 mm to 5 mm HAZ widths were identified for 4 mm plates. In addition, the region of HAZ is determined based on the hardness test results on the milled plate. The chosen HAZ, where the shear segment is applied, had a limited position variation on two sides of the milled plate according to the hardness test results. Therefore, the employed method, as a compromised solution, is valid. The average thickness, width of shear segment (w_0) and calculated area (A_0) of the shear segment of specimens are shown in Table 7.

3.2. Experimental setup and procedure

An Instron testing machine with a 200 kN capacity was used for the shear tests. A displacement-controlled load with a rate of 0.002 mm/s was employed. 3D digital image correlation (DIC) was used to measure the global displacement and local strain during the experiment. The spatial resolution of the system is approximately 23 μm/pixel. A standard calibration process following the instructions of ARAMIS 2021 was conducted before the test. The calibration deviation was 0.03 pixels, lower than the limiting value of 0.1 pixels. Fig. 7 presents a representative example of the experimental setup.

DIC tracks the displacement field of surface speckle patterns during loading. By comparing images at each loading step, the deformation regarding the displacement and local strain on the specimen surface can be accurately measured. For the critical area, especially with complex geometry, the strain contour plot reveals more information than the traditional measuring method, such as strain gauges and extensometers.

A fine random speckle pattern with small particle size was applied during specimen preparation to ensure sufficient grayscale variation within the small field of view of the DIC system. The DIC system's camera and light source were mounted next to the testing machine. The shooting frequency was 1 Hz. The commercial software ZEISS INSPECT Correlate 2023 was used to analyze experimental data. The subset size and the step size are two parameters that directly affect the resolution of deformation measurements. The step size needs to be adjusted with the subset size to balance coverage and computational efficiency. A larger subset size together with a larger step size contains more speckles and has higher robustness during computation but less spatial resolution, which means less information in the recognition of edges and details. The smaller subset and step size are more sensitive to the local deformation on a small scale and lead to a higher resolution, but the measurements are more prone to noise due to fewer speckles included for computation and have a higher calculation cost due to a higher number of subsets to analyze. Therefore, the size of the subset and the step size for the global surface component were set to 19 pixels and 7 pixels, respectively. A virtual extensometer of 40 mm was established, as shown in Fig. 8(a), to measure the global deformation and generate the load-deformation relationship data, which would be used in the following calibration process of the shear-modified GTN model. Simultaneously, the equivalent strain distribution around the shear segment was measured using inspection points created on the smaller local surface component (Fig. 8(b)). For this shear component, the subset size and step size were adjusted to 13 pixels and 5 pixels. The recorded local equivalent strain would be adopted for the following validation process. Given that the width of the shear segment was approximately 3 mm (about 130 pixels), the spatial resolution was sufficient to ensure the measurement accuracy under such conditions.

3.3. Experimental results of shear tests

Initially, two specimens were designed for each type of welded tube. However, due to fabrication errors, i.e. the shear notch was misaligned with the identified HAZ, 14 specimens were tested in the end. All specimens exhibited the same failure modes as depicted in Fig. 9. The load-deformation curves of all tests are shown in Fig. 10. Note that the load variation does not necessarily mean the difference in HAZ strength, as the width of the shear segment (w_0) varies.

Due to the small size of the shear section, the machining error has a great influence on the mechanical performance of the specimen. The engineering shear stress τ and engineering strain ε_{es} were defined as Eq. (9) and Eq. (10).

$$\tau = P/A_0 \tag{9}$$

$$\varepsilon_{es} = U/w_0 \tag{10}$$

where P is the shear load, and U is the displacement recorded by DIC. A_0 and w_0 are presented in Table 7.

As depicted in Fig. 11, there is no pronounced trend in the engineering shear strength of specimens with the same steel grade but different thicknesses.

As the BM shear tests with the same specimen dimensions are not available, the engineering shear strength ($\tau_{e,HAZ}$) is compared to the ultimate strength of BM ($f_{u,BM}$) provided in the previous study [11]. The results are presented in Fig. 12(a). The shear strength softening in the HAZ is more significant in S700 material, while the difference between S355 and S500 is minor. Regardless of the steel grade, the softening of the 8 mm specimen is always slightly less than that of the other two thicknesses.

The same trend was observed in terms of shear ductility. To exclude the effect of dimensional errors, Fig. 12(b) shows the average engineering shear strain corresponding to the peak load. It can be seen that the ductility of the HAZ decreases with the increase of the steel grade. This trend is similar to that of the BM of all steel grades.

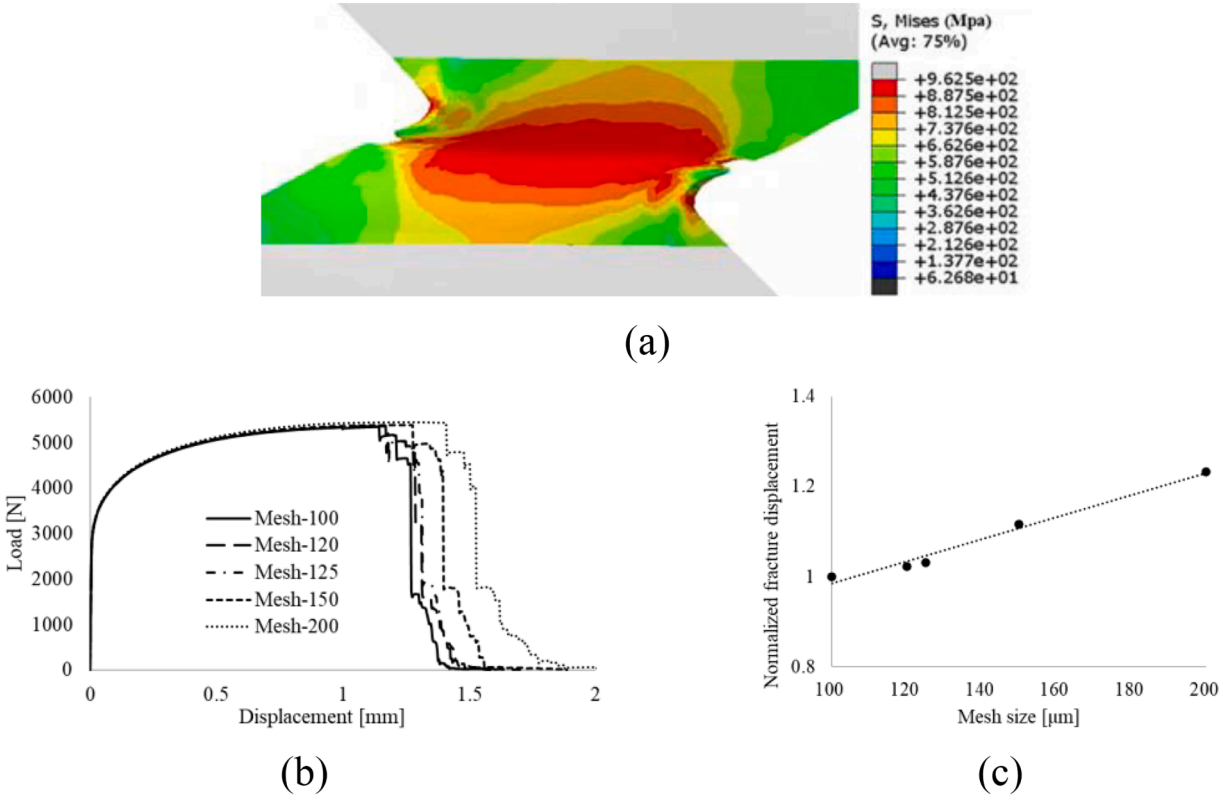

Fig. 16. (a) Shear segment assigned the modified-GTN model (b) Load-displacement curves and (c) normalised fracture displacement under different mesh sizes in the shear segment.

4. FE simulation of HAZ considering the shear-modified GTN model

4.1. FE models

The commercial software ABAQUS:2021 [60] was employed to conduct the FE analysis. The measured dimensions presented in Table 7 were used. The model was divided into several regions with corresponding material properties assigned, as depicted in Fig. 13. The dimensions of HAZ presented in Table 7 were adopted in the FE models. The clamped parts were restricted as the rigid body.

Fixed boundary conditions and displacement loading along the x-axis are applied to the reference points (RP1 and RP2) of the rigid part of the left and right ends of the specimen, respectively. Other degrees of freedom were fully fixed. The detailed boundary conditions are visible in Fig. 13.

Each step was set to be 0.02 s and to carry out a displacement loading of 5 mm. After the explicit analysis, the ratio of kinetic energy to internal energy was kept lower than 0.05, indicating that the simulation results can be considered quasi-static.

4.2. Material properties

The true stress-plastic true strain relationships of BM and WM used in [20] were adopted in this study, as shown in Fig. 14(a) and (b), where the tensile tests of BM (S355, S500 and S700) and corresponding butt-welded joints, method of identifying the HAZ [10], and calibration process of the corresponding property parameters were reported.

The undamaged true stress-plastic true strain relationships of HAZ are shown in Fig. 14(c) according to the parameters reported in [20]. The definition of the modified-GTN model does not reveal the Jacobian matrix which indicates the tangent stiffness related to the stress and strain increment. Therefore, the user-defined material subroutine designed for explicit analysis (VUMAT) in Abaqus was employed. The subroutine follows the Return Mapping Algorithm, assuming the material is in an elastic state to predict the trial stress. If the stress exceeds the yield surface (which means $\Phi > 0$), it is then returned to the yield surface along the normal direction. This step updates the plastic strain, stress, and other relevant variables [61].

When $\Phi >$ tolerance, according to the associated flow rule and Newton iteration method,

$$\Delta\boldsymbol{\varepsilon}^{\boldsymbol{p}} = \Delta\lambda\frac{\partial\Phi}{\partial\boldsymbol{\sigma}} \tag{11}$$

$$\Delta\boldsymbol{\varepsilon}^{p,k+1} = \boldsymbol{\varepsilon}^{p,k+1} - \boldsymbol{\varepsilon}^{p,k} = -\Phi^{k} \Big/ \left(\frac{\partial\Phi}{\partial\boldsymbol{\varepsilon}^{p}}\right)^{k} \tag{12}$$

Thus, the increment of the plastic multiplier can be calculated as Eq. (13):

$$\Delta\lambda^{k+1} = -\left(\frac{\Phi}{\frac{\partial\Phi}{\partial\boldsymbol{\varepsilon}^{p}} : \frac{\partial\Phi}{\partial\boldsymbol{\sigma}}}\right)^{k} \tag{13}$$

Where:

$$\frac{\partial\Phi}{\partial\boldsymbol{\varepsilon}^{p}} = \frac{\partial\Phi}{\partial\boldsymbol{\sigma}}\frac{\partial\boldsymbol{\sigma}}{\partial\boldsymbol{\varepsilon}^{p}} + \frac{\partial\Phi}{\partial f}\frac{\partial f}{\partial\boldsymbol{\varepsilon}^{p}} + \frac{\partial\Phi}{\partial D}\frac{\partial D}{\partial\boldsymbol{\varepsilon}^{p}} + \frac{\partial\Phi}{\partial\sigma_{my}}\frac{\partial\sigma_{my}}{\partial\bar{\varepsilon}_{m}^{p}}\frac{\partial\bar{\varepsilon}_{m}^{p}}{\partial\boldsymbol{\varepsilon}^{p}} \tag{14}$$

Then the increment plastic strain and return step can be calculated as Eq. (15) and Eq. (16):

$$\boldsymbol{\varepsilon}^{p,k+1} = \boldsymbol{\varepsilon}^{p,k} + \Delta\boldsymbol{\varepsilon}^{p,k+1} \tag{15}$$

$$\boldsymbol{\sigma}_{\text{trial}}^{k+1} = \boldsymbol{\sigma}_{\text{trial}}^{k} + \frac{\partial\boldsymbol{\sigma}}{\partial\boldsymbol{\varepsilon}^{p}}\left(\Delta\boldsymbol{\varepsilon}^{p,k+1}\right) \tag{16}$$

Then the other variables can be updated. The iteration should

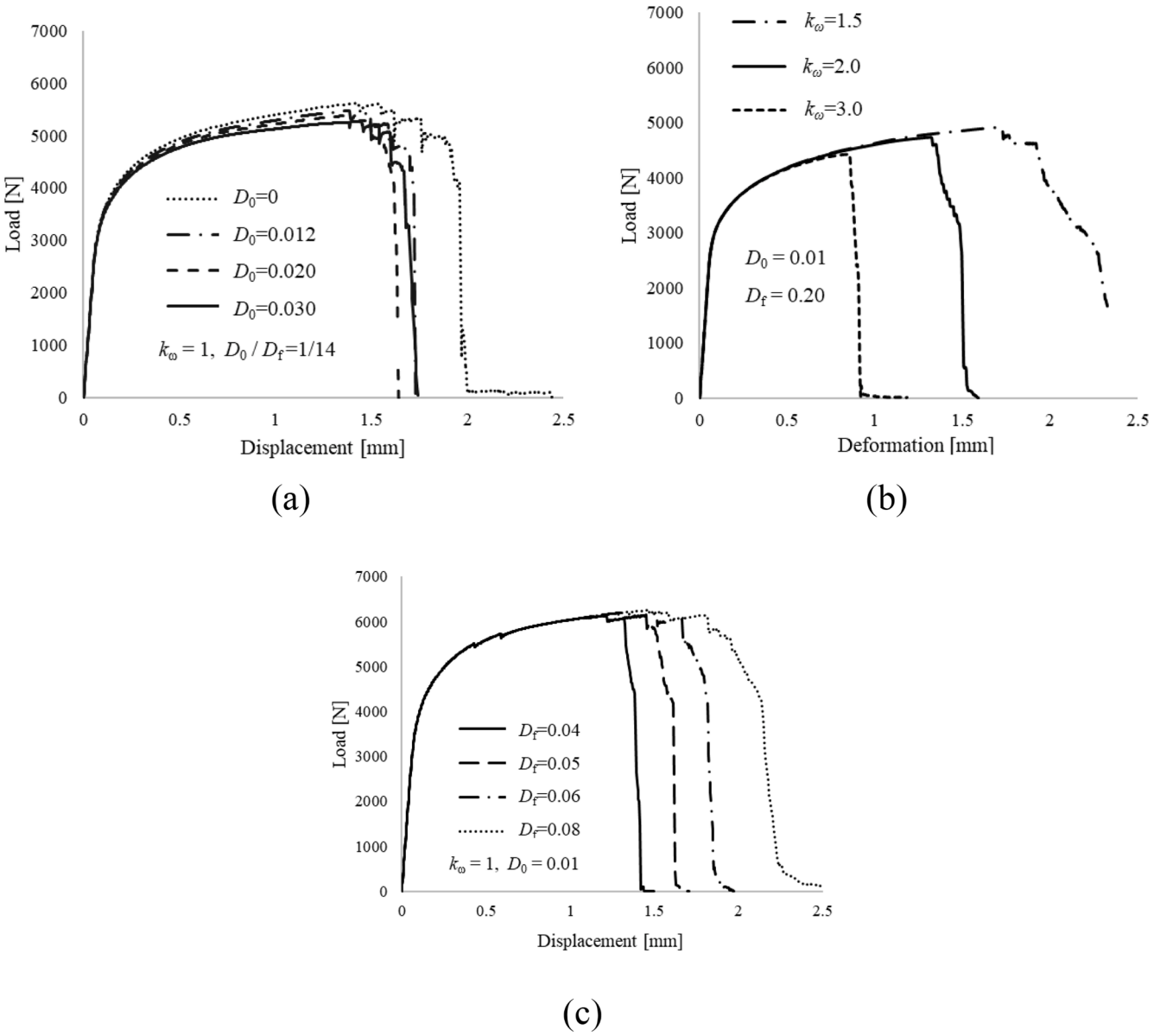

Fig. 17. (a) Load-displacement of S700t5 model with various D_0, (b) S355t10 model with various k_ω and (c) S700t8 model with various D_f.

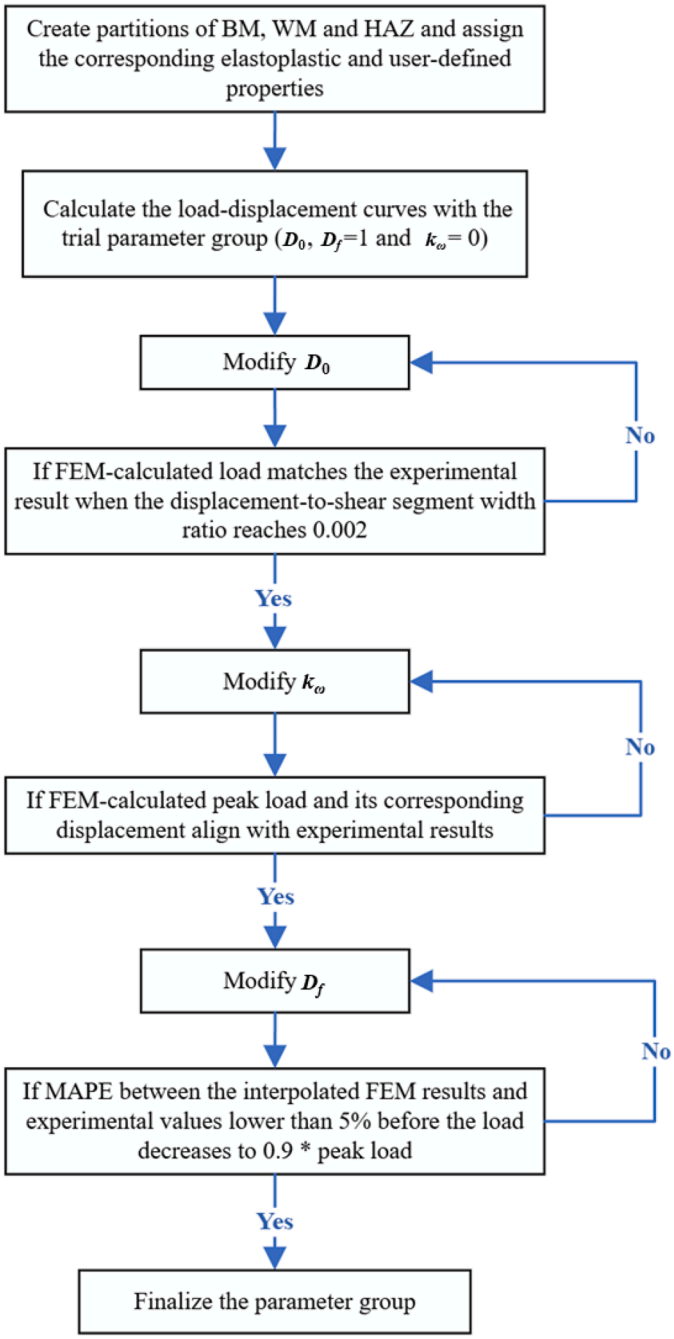

Fig. 18. Flowchart of the calibration process.

Table 8
Parameters in different fracture criteria.

Fracture criteria	D_0	k_ω	D_f	Other parameters
Eq. (7)	0.04	0.5	0.110	–
Eq. (8)	0.04	0.5	0.160	Refer to Table 4

continue until Φ^{k+1} is less than the tolerance. For the possible situation where the VVF approaches zero, the value of q_1 may approach infinity, so a cut-off maximum value should be set in the program to ensure no excessive distortion in the model elements.

The material properties of the WM, BM, and HAZ were assigned to the corresponding regions, as shown in Fig. 13. Since the HAZ2 region remained in the elastic deformation stage during the entire loading process, the shear-modified GTN model was applied only to the HAZ1 region to improve computational efficiency, while damage evolution in HAZ2 was not considered.

4.3. Sensitivity of mesh size

C3D8R meshes were used in this analysis. From previous studies, it is evident that the GTN model is sensitive to mesh size and the larger stress concentration at the onset of element deletion leads to a more serious mesh sensitivity [62–64]. As the mesh size decreases, the load-displacement curves show a clear trend towards convergence. However, with the same parameters, increasing the mesh size delays the model's element deletion and fracture. Convergence cannot be obtained and different mesh distribution leads to different crack propagation paths. In this case, the fracture surface of the shear segment would be different with the mesh size of 250 μm, 125 μm and 100 μm as shown in Fig. 15.

The larger element presents an averaged distribution of damage within the mesh size. This reduces stress concentration effects, thereby delaying the onset of element deletion. However, as the mesh size decreases, the damage can become overly concentrated, leading to unreasonable crack propagation patterns and inaccurate predictions. Besides, the overly fine mesh can cause other numerical problems such as stress oscillations and computational divergence [65]. To solve the problem, the same mesh size should be used in subsequent applications to ensure the accuracy of fracture prediction. In this study, the modified GTN model is assigned to shear segments, shown in Fig. 16(a), with the same parameters and different mesh sizes. The loading results show that the 100 to 200 μm mesh can converge in the stress and strain before the onset of element deletion but it can be seen from Fig. 16(c) that the normalized fracture displacement is nearly linear with the element size, and convergence cannot be achieved. When the mesh size is 80 μm, the failure mode of the model changes dramatically, so the 100 μm mesh calculation is used in the subsequent calibration work.

5. Calibration of shear-modified GTN model

5.1. Parameters calibration procedure

A parametric study on shear specimens has revealed the effects of parameters on the macroscopic mechanical response.

The parameter D_0 is related to the initial shear damage of the material. It prominently influences resistance after the elastic stage. A higher D_0 corresponds to a slower increase in the resistance and a lower peak value as shown in Fig. 17(a).

Fig. 17(b) demonstrates the effect of k_ω on the behaviour of the FE model. The parameter k_ω is associated with the progression of shear damage. Its influence becomes increasingly significant as D accumulates. A larger k_ω leads to an early failure as well as a rapid decline after peak load. Due to the swifter degradation of the remaining elements after the onset of fracture, the resistance drops off more rapidly compared with that of smaller k_ω.

The parameter D_f does not affect the calculations before element deletion occurs and only determines the individual element deletion. Consequently, a smaller D_f value results in an earlier element deletion, leading to an earlier fracture failure and a more rapid decrease of resistance after the onset of fracture, see Fig. 17(c).

Therefore, the tangent stiffness in the hardening phase, peak load, fracture displacement and post-fracture behaviour of shear specimens are collectively influenced by these three parameters.

The calibration process was conducted as shown in a flow chart in Fig. 18. Mean Absolute Percentage Error (MAPE) calculated as Eq. (17) was used as the index to evaluate the errors of simulated and experimental results. Due to observed instability in simulating post-failure behaviour, load-displacement data before the load decreased to 90 % of the maximum value was determined for error estimation.

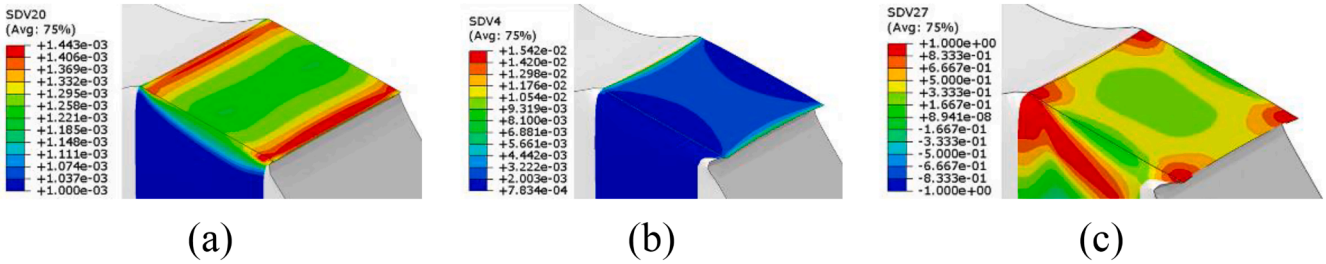

Fig. 19. (a) shear damage (b) VVF and (c) Lode parameter ξ on the shear segment cross-section before the first element being deleted in the calibration result of S700t5.

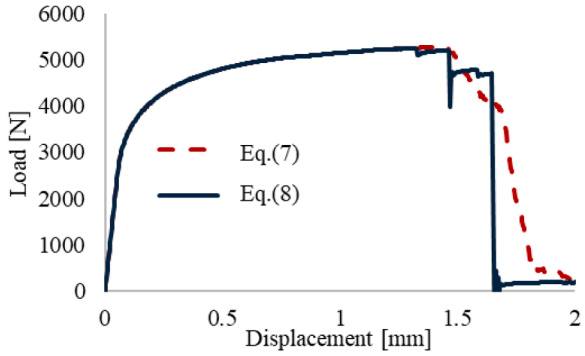

Fig. 20. Calibrated results of S700t5 with different definitions of D_{eff}.

$$\text{MAPE} = \frac{\sqrt{\frac{1}{n}\sum_{i=1}^{n}\left(y_{\text{exp},i} - y_{\text{fem},i}\right)^2}}{y_{\text{exp,max}}} \tag{17}$$

5.2. Model calibration results

Taking S700t5 for instance, the simulation results of fracture criteria in Eq. (7) and Eq. (8) are compared using the same D_0, k_ω, and different D_f after calibration as displayed in Table 8. The shear damage gradient, VVF gradient, and Lode parameter gradient during the loading process can be significantly large near the shear segment's edge as shown in Fig. 19. In the circumstance of adopting Eq. (8), after the edge elements with ξ near 0.95 are deleted, it will take a larger loading displacement to delete the elements at the center, leading to unreasonable stepped post-fracture curves compared with the curve of Eq. (7), as shown in Fig. 20.

5.2.1. Comparison of calibration results and test data

As shown by the calibration results of the shear specimens in Fig. 21, the shear-modified GTN model can simulate the mechanical performance of the specimens under shear load. However, the descending part of the curve is not stable in the post-fracture stage. The parameters calibrated are shown in Table 9.

Moreover, in the calibration process, it was found that the calibration results strongly depend on the undamaged matrix property of the HAZ, the difference in shear segment width, and the width of the HAZ. It is possible to simulate the fracture displacement by adjusting the shear parameters but controlling the slope of the descending part after the fracture needs further improvement.

5.2.2. Verification of the modified GTN model based on the test data (local strain)

The local strains measured by 3D DIC were used to verify the FE model. The equivalent strains were measured from FE models and compared with those from 3D DIC at five inspection points (Fig. 22). Additionally, since the DIC identification is based on a 13-pixel subset, which is approximately 0.3 mm, the average value of integration points within a 0.3 mm range in the FE model was taken as the representative simulated value, as marked in Fig. 22(a).

The comparison in Fig. 23 demonstrates that the simulated values generally align well with the experimental data. The number at the end of the legend name denotes the measuring displacement corresponding to the limitation of DIC recognition, as marked in Fig. 21. In addition to the inherent limitations of the local fracture model, discrepancies in the observation of local strains could also arise from differences in specimen cutting and model dimensions.

5.3. Conservative solution

The GTN model parameters obtained from the calibration exhibit an unclear correlation with the strength or the tube thickness, resulting from several potential factors. Firstly, errors in measuring the width and thickness of the shear segment may cause discrepancies in calibration results. Secondly, the possible heat input variation along the welding seam may result in varying HAZ width and strength. Although hardness is obtained on the edges of milled plates, the risk of HAZ variation at the center of the plate still exists. This difference in specimens and FE model directly affects the calibrated equivalent mechanical property of the shear segment. Finally, the shear segment was cut from the region next to the weld seam. It is possible that a limited portion of BM or WM might be involved in the tested shear segment. However, the focus of the present study is on the behaviour of the entire region, excluding the fracture propagation. The potential small portion of the BM or WM might greatly influence the fracture initiation and propagation, but not the plastic hardening behaviour. The calibrated parameters are still valid.

Considering the abovementioned issues, three groups of parameters that can conservatively estimate the mechanical behaviour of shear specimens with strength grades of S355, S500 and S700 were proposed for practical applications. The determined parameter groups are shown in Table 10. The conservative predictions are compared to experiments in Fig. 24.

The estimated ultimate load carrying capacity from Fig. 24 are compared in Table 11 with the experimental values for each specimen. It can be seen that the estimated ultimate load carrying capacity is in close agreement (approximately 5 %) with the experimental values with a coefficient of variation (COV) of 0.0414.

4. Conclusions and future work

In this study, the shear-modified GTN model was calibrated using shear test results from the heat-affected zones (HAZ) of S355, S500, and S700 butt-welded cold-formed tubes. Parameters related to tensile fracture were adopted from previous GTN model calibrations, while shear damage parameters were determined by integrating both experimental and numerical results for each material investigated. As a result, the modified model is applicable to both tensile and shear fracture. The main findings are as follows:

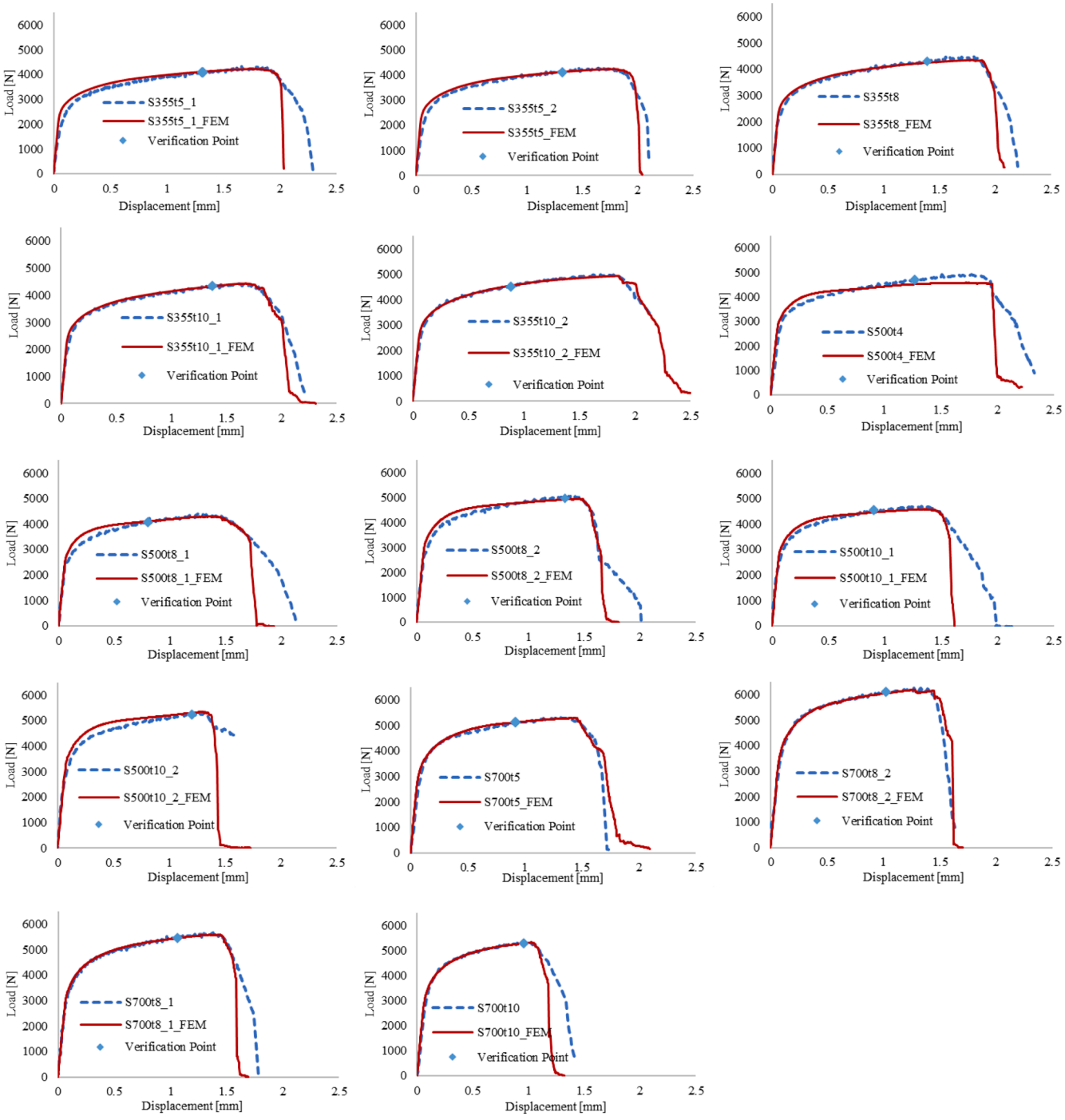

Fig. 21. Calibration results.

Table 9
Calibration results.

Specimen Code	D_0	D_f	k_ω	MAPE
S355t5_1	0.08	0.152	0.4	0.0354
S355t5_2	0.08	0.151	0.4	0.0379
S355t8	0.07	0.138	0.3	0.0212
S355t10_1	0.06	0.120	0.3	0.0203
S355t10_2	0.006	0.360	2	0.0145
S500t4	0.001	0.008	0.8	0.0448
S500t8_1	0.001	0.003	0.4	0.0376
S500t8_2	0.001	0.006	1	0.0340
S500t10_1	0.001	0.0022	0.3	0.0330
S500t10_2	0.015	0.028	0.3	0.0406
S700t5	0.04	0.110	0.5	0.0240
S700t8_1	0.001	0.0023	0.5	0.0121
S700t8_2	0.01	0.05	1	0.0162
S700t10	0.02	0.041	0.5	0.0225

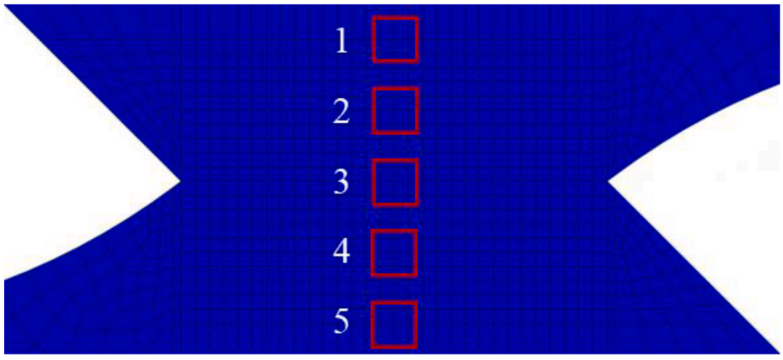

(a)

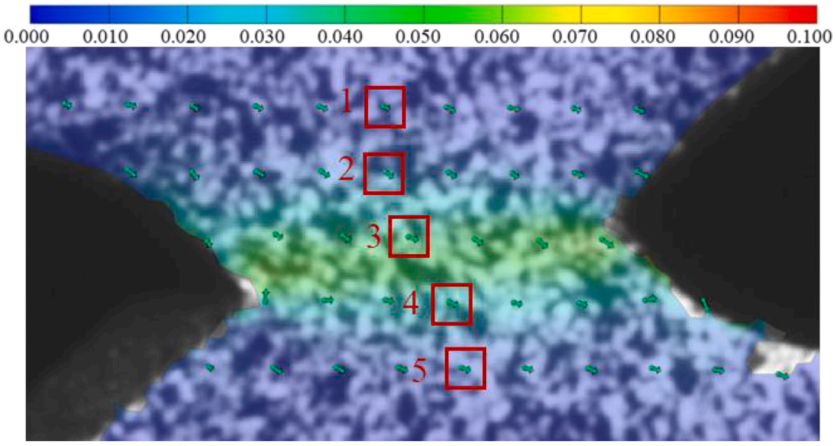

(b)

Fig. 22. (a) Average calculation range in FE model and (b) corresponding positions of inspection points in specimens.

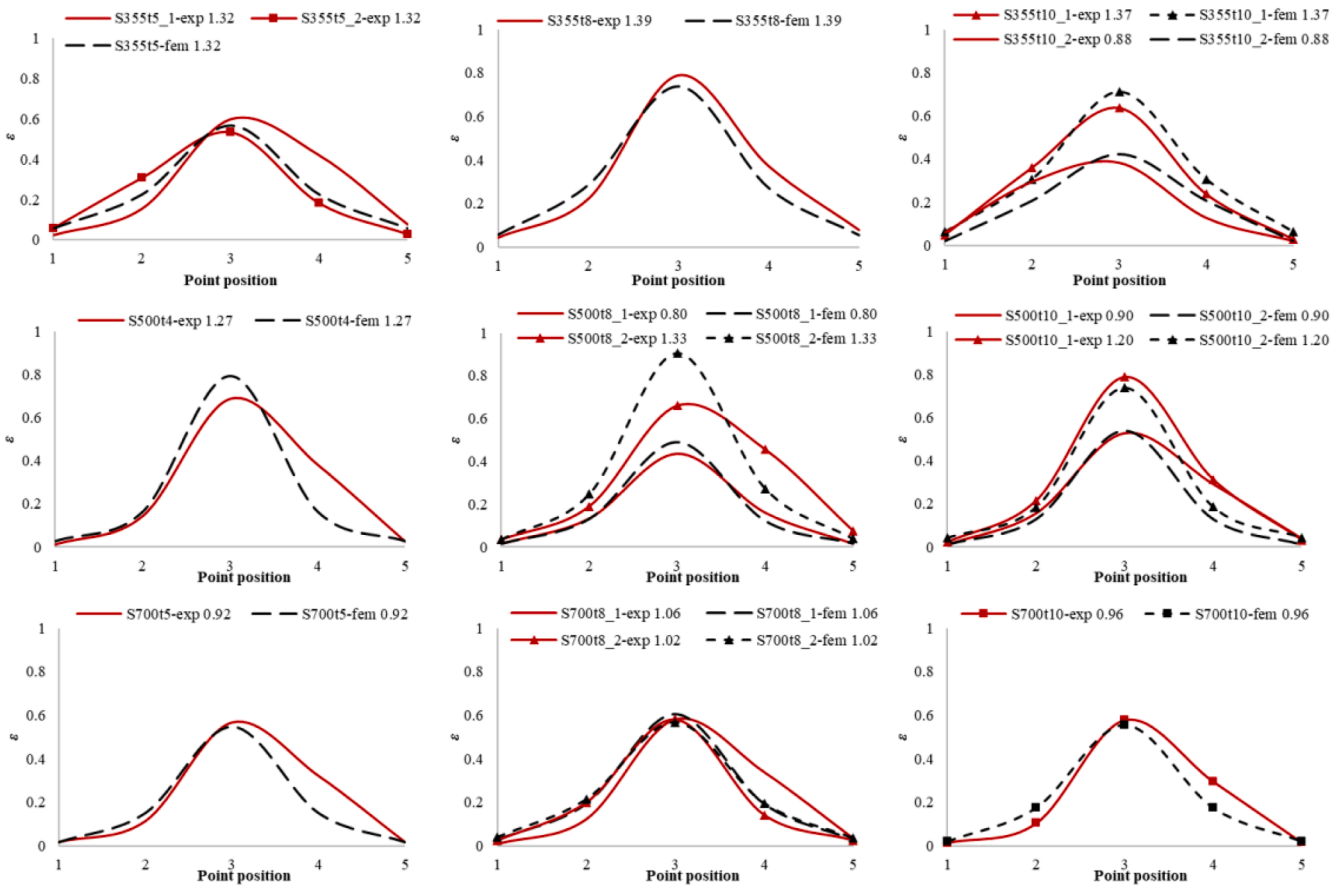

Fig. 23. Comparison of experimental and simulation results of equivalent strain in the central line of the shear segment.

Table 10
Conservative parameter groups for S355, S500 and S700.

Strength grade	D_0	D_f	k_ω
S355	0.080	0.151	0.4
S500	0.015	0.028	0.3
S700	0.040	0.090	0.5

1. The shear strength of HAZ decreases significantly in the investigated S700 butt-welded connections compared to those of S500 and S355. The shear ductility of HAZ decreases with increasing steel grade.
2. The shear-modified GTN model effectively captures the equivalent material behavior of the HAZ in HSS butt welds under shear-dominated stress states. The model demonstrates strong agreement with both load-deformation relationships and local equivalent strain fields. Furthermore, the calibrated shear-modified GTN model is also applicable to tensile-dominated stress states.
3. The parameters D_0 and k_ω affect the shear damage accumulation and the ultimate resistance. The parameter D_f determines the onset of failure. The value of D_f is affected by D_0, k_ω and the mesh size of the model.
4. The steel grade (S355, S500, and S700) and thickness (4 mm/5 mm, 8 mm, and 10 mm) of the welded tube do not have significant influences on the parameters of shear damage. A group of parameters is recommended for each steel grade as a conservative practical solution to evaluate the mechanical behaviour of HAZ in HSS butt welds.

Future research focuses on the following four aspects to increase the applicability of the shear-modified GTN model.

(a) Variations in heat input during the welding process leads to differences in the mechanical properties and distribution of HAZ. A more comprehensive investigation concerning a broader range of welding parameters should be conducted to understand their effects on the HAZ and to enhance the applicability of the shear-modified GTN model.
(b) The shear behaviour of HAZ in the thickness (e.g. for punching shear failure of tubular joints) and welding (e.g. for butt-welded tubes in torsion) directions was not covered in this study. Further investigations are required.
(c) The calibrated shear-modified model should be verified against tests of different welded joints considering the differences between coupon and joint specimens, such as the residual stress, the scatter of HAZ properties, and welding defects.

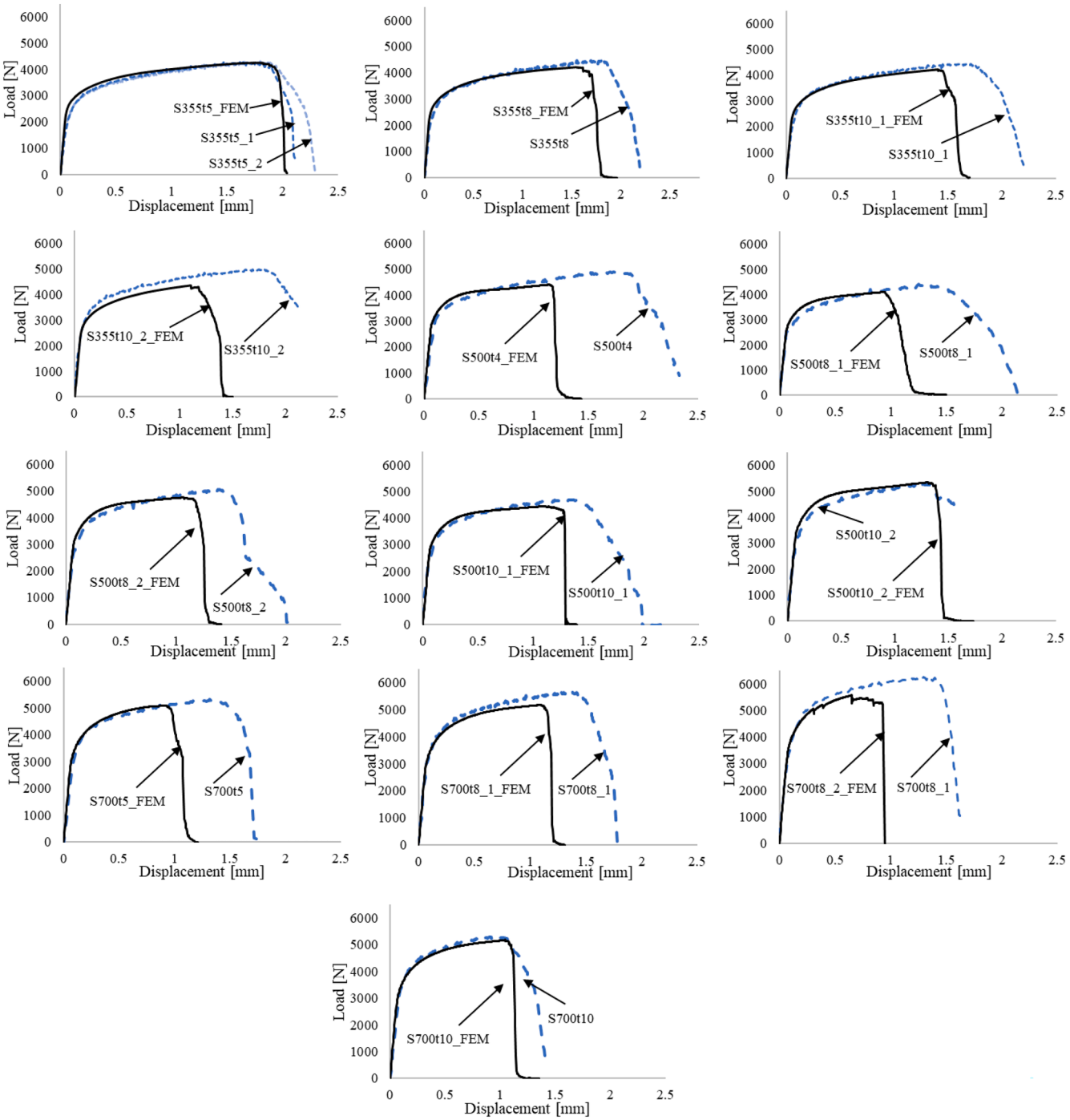

Fig. 24. Conservative simulation results by FEM and the corresponding experimental results.

Table 11
Comparison of the estimated ultimate load carrying capacity and the experimental values.

Specimen code	P_{ult_exp} (N)	P_{ult_FE} (N)	P_{ult_FE} / P_{ult_exp}
S355t5_1	4334	4244	0.979
S355t5_2	4288	4244	0.990
S355t8	4465	4213	0.944
S355t10_1	4437	4220	0.951
S355t10_2	4974	4365	0.878
S500t4	4913	4402	0.896
S500t8_1	4414	4300	0.974
S500t8_2	5059	4756	0.940
S500t10_1	4711	4447	0.944
S500t10_2	5322	5350	1.005
S700t5	5323	5099	0.958
S700t8_1	5659	5171	0.914
S700t8_2	6247	5561	0.890
S700t10	5311	5195	0.978
Mean			0.946
COV			0.0414

(d) HAZ in different HSS welded connections may exhibit various mechanical and microstructural properties under the same welding process. More tests on specimens with a wider range of grades, thicknesses, and delivery conditions are needed to increase the reliability of the proposed parameters.

CRediT authorship contribution statement

Yize Gao: Writing – original draft, Visualization, Methodology, Investigation, Formal analysis. **Rui Yan:** Writing – review & editing, Visualization, Methodology, Data curation. **Milan Veljkovic:** Writing – review & editing, Supervision. **Kristo Mela:** Writing – review & editing, Supervision. **Guo-Qiang Li:** Writing – review & editing, Supervision, Methodology. **Yan-Bo Wang:** Writing – review & editing, Supervision. **Xiao-Ling Zhao:** Writing – review & editing, Supervision, Resources, Methodology, Conceptualization.

Declaration of competing interest

The authors declare that they do not have any commercial or associative interest that represents a conflict of interest in connection with the work submitted.

Acknowledgements

The authors would like to thank the company SSAB Europe for the financial support. And this work was also supported by the National Natural Science Foundation of China (52020105004).

Data availability

Data will be made available on request.

References

[1] X. Liu, S. Yan, J. Zhou, K.J.R. Rasmussen, G.G. Deierlein, Measurement of strengths and fracture initiation strains of weld metal and HAZ in steel joints using miniature coupons, Eng. Fract. Mech. 307 (2024).
[2] M. Rahman, W. Maurer, W. Ernst, R. Rauch, N. Enzinger, Calculation of hardness distribution in the HAZ of micro-alloyed steel, Weld. World 58 (6) (2014) 763–770.
[3] D.D. Jan Schubnell, Majid Farajian, Determination of the static, dynamic and cyclic properties of the heat affected zone for different steel grades, Mater. Test. 61 (7) (2019) 635–642.
[4] M.M. Ran, F.F. Sun, G.Q. Li, Y.B. Wang, Mechanical properties of mismatched high strength steel butt joints with three softened/hardened strength distribution patterns, Thin-Walled Struct. 146 (2020).
[5] J. Górka, Microstructure and properties of the high-temperature (HAZ) of thermo-mechanically treated S700MC high-yield-strength steel, Mater. Technol. 50 (4) (2015) 617–621.
[6] W. Maurer, W. Ernst, R. Rauch, R. Vallant, N. Enzinger, Evaluation of the factors influencing the strength of HSLA steel weld joint with softened HAZ, Weld. World 59 (6) (2015) 809–822.
[7] F. Sun, M. Ran, G. Li, R.Y. Xiao, Y. Wang, Experimental and numerical study of high-strength steel butt weld with softened HAZ, Proc. Inst. Civ. Eng. - Struct. Build. 171 (8) (2018) 583–597.
[8] M.M. Ran, F.F. Sun, G.Q. Li, A. Kanvinde, Y.B. Wang, R.Y. Xiao, Experimental study on the behavior of mismatched butt welded joints of high strength steel, J. Constr. Steel. Res. 153 (2019) 196–208.
[9] M. Amraei, S. Afkhami, V. Javaheri, J. Larkiola, T. Skriko, T. Björk, X.L. Zhao, Mechanical properties and microstructural evaluation of the heat-affected zone in ultra-high strength steels, Thin-Walled Struct. 157 (2020).
[10] R. Yan, H. El Bamby, M. Veljkovic, H. Xin, F. Yang, A method for identifying the boundary of regions in welded coupon specimens using digital image correlation, Mater. Des. 210 (2021).
[11] R. Yan, K. Mela, F. Yang, H. El Bamby, M. Veljkovic, Equivalent material properties of the heat-affected zone in welded cold-formed rectangular hollow section connections, Thin-Walled Struct. 184 (2023).
[12] R. Yan, H. Xie, F. Yang, M. Veljkovic, X.L. Zhao, A macro prediction model for butt-welded (U)HSS connections with softened HAZ, J. Constr. Steel. Res. 211 (2023).
[13] J. Xue, W. Guo, Y. Zhang, M. Xia, Q. Jia, J. Chi, J. Shi, Y. Wu, H. Zhang, Local microstructure and mechanical characteristics of HAZ and tensile behavior of laser welded QP980 joints, Mater. Sci. Eng. 854 (2022).
[14] C. Chen, S.P. Chiew, M.S. Zhao, C.K. Lee, T.C. Fung, Welding effect on tensile strength of grade S690Q steel butt joint, J. Constr. Steel. Res. 153 (2019) 153–168.
[15] M.T. Chen, Y. Pan, F. Ren, H. Cao, M. Lai, J. Zhang, Experimental investigation and predictive model on tensile behavior of corroded high-strength steel and butt-welded connections, Thin-Walled Struct. 210 (2025).
[16] A.M. El-Batahgy, Influence of HAZ microstructure and stress concentration on fatigue strength of welded structural steel, Mater. Lett. 21 (5–6) (1994) 415–423.
[17] S. Kim, D. Kang, T.W. Kim, J. Lee, C. Lee, Fatigue crack growth behavior of the simulated HAZ of 800MPa grade high-performance steel, Mater. Sci. Eng. 528 (6) (2011) 2331–2338.
[18] S. Tsutsumi, R. Fincato, P. Luo, M. Sano, T. Umeda, T. Kinoshita, T. Tagawa, Effects of weld geometry and HAZ property on low-cycle fatigue behavior of welded joint, Int. J. Fatigue 156 (2022).
[19] Y. Zhang, L. Hu, C. Shen, X.L. Zhao, Study on fatigue behavior of butt-welded high-strength steel connections with surface cracks, Thin-Walled Struct. 200 (2024).
[20] R. Yan, H. Xin, K. Mela, H. El Bamby, M. Veljkovic, Fracture simulation of welded RHS X-joints using GTN damage model, Adv. Struct. Eng. 26 (12) (2022) 2140–2159.
[21] T.W. Ling, X.L. Zhao, R. Al-Mahaidi, J.A. Packer, Investigation of block shear tear-out failure in gusset-plate welded connections in structural steel hollow sections and very high strength tubes, Eng. Struct. 29 (4) (2007) 469–482.
[22] T.W. Ling, X.L. Zhao, R. Al-Mahaidi, J.A. Packer, Investigation of shear lag failure in gusset-plate welded structural steel hollow section connections, J.Construct. Steel Res. 63 (3) (2007) 293–304.
[23] S. Han, Y. Chang, C.Y. Wang, H. Dong, A comprehensive investigation on the damage induced by the shearing process in DP780 steel, J. Mater. Process. Technol. 299 (2022).
[24] Z.Q. Zhou, Z.C. Du, X. Wang, H.L. Jiang, Q. Zhou, Y.L. Zhang, Y.Z. Liu, P.Z. Zhang, Micro defects formation and dynamic response analysis of steel plate of quasi-cracking area subjected to explosive load, Def. Technol. 31 (2024) 580–593.
[25] F.A. McClintock, A criterion for ductile fracture by the growth of holes, J. Appl. Mech. 35 (2) (1968) 363–371.
[26] J.R. Rice, D.M. Tracey, On the ductile enlargement of voids in triaxial stress fields, J. Mech. Phusics Solid. 17 (3) (1969) 125–217.
[27] A.L. Gurson, Continuum theory of ductile rupture by void nucleation and growth: part I - yield criteria and flow rules for porous ductile media, J. Eng. Mater. Technol. 76 (1977) 2–15.
[28] V. Tvergaard, Influence of voids on shear band instabilities under plane strain conditions, Int. J. Fract. 17 (4) (1981) 389–407.
[29] V. Tvergaard, A. Needleman, Analysis of the cup-cone fracture in a round tensile bar, Acta Met. 32 (1) (1984) 157–169.
[30] F. Fritzen, S. Forest, T. Böhlke, D. Kondo, T. Kanit, Computational homogenization of elasto-plastic porous metals, Int. J. Plast. 29 (2012) 102–119.
[31] T.S. Cao, E. Maire, C. Verdu, C. Bobadilla, P. Lasne, P. Montmitonnet, P. O. Bouchard, Characterization of ductile damage for a high carbon steel using 3D X-ray micro-tomography and mechanical tests – application to the identification of a shear modified GTN model, Comput. Mater. Sci. 84 (2014) 175–187.
[32] J. Faleskog, X. Gao, F. Shin, Cell model for nonlinear fracture analysis - I. Micromechanics calibration, Int. J. Fract. 89 (1998) 355–373.
[33] R. Yan, H. Xin, M. Veljkovic, Ductile fracture simulation of cold-formed high strength steel using GTN damage model, J. Constr. Steel. Res. 184 (2021).
[34] B.V. Farahani, R. Amaral, J. Belinha, P.J. Tavares, P. Moreira, A GTN failure analysis of an AA6061-T6 Bi-failure specimen, Procedia Struct. Integr. 5 (2017) 981–998.
[35] G. Cricrì, A consistent use of the Gurson-Tvergaard-Needleman damage model for the R-curve calculation, Frat. Integrità Strutt. 7 (24) (2013) 161–174.
[36] S. Acharyya, S. Dhar, A complete GTN model for prediction of ductile failure of pipe, J. Mater. Sci. 43 (6) (2008) 1897–1909.
[37] J. Liu, S. Yan, X. Zhao, Simulation of fracture of a tubular X-joint using a shear-modified Gurson–Tvergaard–Needleman model, Thin-Walled Struct. 132 (2018) 120–135.

[38] F.J.P. Reis, L. Malcher, F.M. Andrade Pires, J.M.A. Ceśar de Sa, A comparison of shear mechanisms for the prediction of ductile failure under low stress triaxiality, Int. J. Struct. Integr. 1 (4) (2010) 314–331.
[39] X. Li, Z. Chen, C. Dong, Failure and forming quality study of metallic foil blanking with different punch-die clearances, Int. J. Adv. Manuf. Technol. 115 (9–10) (2021) 3163–3176.
[40] J. Kim, X. Gao, T.S. Srivatsan, Modeling of void growth in ductile solids: effects of stress triaxiality and initial porosity, Eng. Fract. Mech. 71 (3) (2004) 379–400.
[41] K. Nahshon, J.W. Hutchinson, Modification of the Gurson Model for shear failure, Eur. J. Mech. - A/Solids 27 (1) (2008) 1–17.
[42] A. Weck, D.S. Wilkinson, H. Toda, E. Maire, 2D and 3D visualization of ductile fracture, Adv. Eng. Mater. 8 (6) (2006) 469–472.
[43] F. McClintock, S. Kaplan, C. Berg, Ductile fracture by hole growth in shear bands, Int. J. Fract. Mech. 2 (4) (1966) 614–627.
[44] K.L. Nielsen, J. Dahl, V. Tvergaard, Collapse and coalescence of spherical voids subject to intense shearing: studied in full 3D, Int. J. Fract. 177 (2) (2012) 97–108.
[45] Y. Zhang, J. Zheng, F. Shen, D. Li, S. Münstermann, W. Han, S. Huang, T. Li, Ductile fracture prediction of HPDC aluminum alloy based on a shear-modified GTN damage model, Eng. Fract. Mech. 291 (2023).
[46] R.O. Santos, L.P. Moreira, M.C. Butuc, G. Vincze, A.B. Pereira, Damage analysis of third-generation advanced high-strength steel based on the Gurson–Tvergaard–Needleman (GTN) model, Metals 12 (2) (2022).
[47] L. Xue, Constitutive modeling of void shearing effect in ductile fracture of porous materials, Eng. Fract. Mech. 75 (11) (2008) 3343–3366.
[48] C. Butcher, Z.T. Chen, A void coalescence model for combined tension and shear, Model. Simul. Mater. Sci. Eng. 17 (2) (2009).
[49] C. Butcher, Z. Chen, A. Bardelcik, M. Worswick, Damage-based finite-element modeling of tube hydroforming, Int. J. Fract. 155 (1) (2009) 55–65.
[50] J. Zhou, X. Gao, J.C. Sobotka, B.A. Webler, B.V. Cockeram, On the extension of the Gurson-type porous plasticity models for prediction of ductile fracture under shear-dominated conditions, Int. J. Solids. Struct. 51 (18) (2014) 3273–3291.
[51] R. Yan, Heat-affected Zone in Welded Cold-Formed Rectangular Hollow Section Joints, Delft University of Technology, 2023.
[52] L. Malcher, F.M. Andrade Pires, J.M.A. César de Sá, An extended GTN model for ductile fracture under high and low stress triaxiality, Int. J. Plast. 54 (2014) 193–228.
[53] W. Jiang, Y. Li, J. Su, Modified GTN model for a broad range of stress states and application to ductile fracture, Eur. J. Mech. - A/Solids 57 (2016) 132–148.
[54] H. Wu, X. Zhuang, Z. Zhao, Extended GTN model for predicting ductile fracture under a broad range of stress states, Int. J. Solids. Struct. (2022) 239–240.
[55] S. Han, Y. Chang, C. Wang, Y. Han, H. Dong, Experimental and numerical investigations on the damage induced in the shearing process for QP980 steel, Materials 15 (9) (2022).
[56] S. Wang, Z. Chen, C. Dong, Tearing failure of ultra-thin sheet-metal involving size effect in blanking process: analysis based on modified GTN model, Int. J. Mech. Sci. 133 (2017) 288–302.
[57] P.J. Zhao, Z.H. Chen, C.F. Dong, Failure analysis based on microvoids damage model for DP600 steel on in-situ tensile tests, Eng. Fract. Mech. 154 (2016) 152–168.
[58] Z. He, H. Zhu, Y. Hu, An improved shear modified GTN model for ductile fracture of aluminium alloys under different stress states and its parameters identification, Int. J. Mech. Sci. 192 (2021).
[59] EN10219-1, European Standard, cold formed welded structural hollow sections of non-alloy and fine grain steel, part 1: technical delivery conditions, 2006.
[60] D. Systèmes, Dassault Systèmes Simulia Corp., Providence, RI, USA, 2021.
[61] N. Aravas, On the numerical integration of a class of pressure-dependent plasticity models, Int. J. Numer. Methods Eng. 24 (7) (2005) 1395–1416.
[62] Y. Yin, T. Yang, W. Qin, Y. Lu, Y. Gu, Calibration of GTN model for fracture analysis of steel plates with holes, J. Constr. Steel. Res. 215 (2024).
[63] V. Brinnel, J. Langenberg, F. Kordtomeikel, Y. Di, S. Münstermann, Numerical derivation of strain-based criteria for ductile failure: discussions on sensitivity and validity, Eng. Fract. Mech. 148 (2015) 421–440.
[64] P. Han, P. Cheng, S. Yuan, Y. Bai, Characterization of ductile fracture criterion for API X80 pipeline steel based on a phenomenological approach, Thin-Walled Struct. 164 (2021).
[65] V. Espeseth, D. Morin, T. Børvik, O.S. Hopperstad, A gradient-based non-local GTN model: explicit finite element simulation of ductile damage and fracture, Eng. Fract. Mech. 289 (2023).